

RESEARCH ARTICLE

10.1029/2018JB015998

Key Points:

- New global inventories of oceanic basement depths and heat flow are assembled
- An objective assessment of thermal models with increasingly complex parameterizations is carried out
- Optimal thermal structure for oceanic lithosphere is identified, and its implications examined

Supporting Information:

- Supporting Information S1
- Data Set S1
- Data Set S2
- Data Set S3
- Data Set S4
- Data Set S5
- Data Set S6

Correspondence to:

F. D. Richards, M. J. Hoggard and N. J. White,
frichards@schmidtschneffellows.org;
mark_hoggard@fas.harvard.edu;
njw10@cam.ac.uk

Citation:

Richards, F. D., Hoggard, M. J., Cowton, L. R., & White, N. J. (2018). Reassessing the thermal structure of oceanic lithosphere with revised global inventories of basement depths and heat flow measurements. *Journal of Geophysical Research: Solid Earth*, 123, 9136–9161. <https://doi.org/10.1029/2018JB015998>

Received 25 APR 2018

Accepted 17 AUG 2018

Accepted article online 22 AUG 2018

Published online 9 OCT 2018

Reassessing the Thermal Structure of Oceanic Lithosphere With Revised Global Inventories of Basement Depths and Heat Flow Measurements

F. D. Richards^{1,2} , M. J. Hoggard² , L. R. Cowton³ , and N. J. White¹ 

¹Bullard Laboratories, Department of Earth Sciences, Madingley Rise, Cambridge, UK, ²Department of Earth and Planetary Sciences, Harvard University, Cambridge, MA, USA, ³ASI Data Science, London, UK

Abstract Half-space cooling and plate models of varying complexity have been proposed to account for changes in basement depth and heat flow as a function of lithospheric age in the oceanic realm. Here, we revisit this well-known problem by exploiting a revised and augmented database of 2,028 measurements of depth to oceanic basement, corrected for sedimentary loading and variable crustal thickness, and 3,597 corrected heat flow measurements. Joint inverse modeling of both databases shows that the half-space cooling model yields a mid-oceanic axial temperature that is $> 100^{\circ}\text{C}$ hotter than permitted by petrologic constraints. It also fails to produce the observed flattening at old ages. Then, we investigate a suite of increasingly complex plate models and conclude that the optimal model requires incorporation of experimentally determined temperature- and pressure-dependent conductivity, expansivity, and specific heat capacity, as well as a low-conductivity crustal layer. This revised model has a mantle potential temperature of $1300 \pm 50^{\circ}\text{C}$, which honors independent geochemical constraints and has an initial ridge depth of 2.6 ± 0.3 km with a plate thickness of 135 ± 30 km. It predicts that the maximum depth of intraplate earthquakes is bounded by the 700°C isothermal contour, consistent with laboratory creep experiments on olivine aggregates. Estimates of the lithosphere-asthenosphere boundary derived from studies of azimuthal anisotropy coincide with the $1175 \pm 50^{\circ}\text{C}$ isotherm. The model can be used to isolate residual depth and gravity anomalies generated by flexural and sub-plate convective processes.

1. Introduction

The observed subsidence and heat flow of oceanic seafloor as a function of age places significant constraints upon the thermal evolution of lithospheric plates (McKenzie, 1967; Turcotte & Oxburgh, 1967). By combining an understanding of this behavior with the depth distribution of intraplate earthquakes, it is possible to make inferences about the rheological properties of oceanic lithosphere that affect the way in which rigid plates transmit elastic stresses and bend under loads (Bry & White, 2007; Craig et al., 2014; McKenzie et al., 2005; Watts & Zhong, 2000). This thermal structure also plays a primary role in the generation of convective instabilities, anisotropic fabrics, and the potential pooling of melts at the lithosphere-asthenosphere boundary (Burgos et al., 2014; Stern et al., 2015; Turcotte & Schubert, 2002). A quantitative understanding of the average behavior through time enables accurate residuals to be isolated that relate to other geologic processes such as mantle convection and flexure. For example, measurements of oceanic residual depth anomalies play a key role in helping to estimate spatial patterns of dynamic topography, which in turn enables the viscosity and density structure of the upper and lower mantle to be constrained (Hoggard et al., 2017).

In the 1970s, regional and sometimes global compilations of age-depth and heat flow observations were used to build simple quantitative models of the cooling of oceanic lithosphere (Lister, 1972; Parsons & Sclater, 1977). Two principal models were proposed: a half-space model, in which the lithosphere cools and thickens indefinitely as a function of age, and a plate model, in which the lithosphere cools and thickens but approaches a finite thickness controlled by the convective resupply of basal heat, probably related to growth of a Rayleigh-Taylor instability at the base of the plate (Davaille & Jaupart, 1994; Huang & Zhong, 2005; Parsons & McKenzie, 1978; Yuen & Fleitout, 1985). Both models are predicated upon solutions of the heat flow equation for purely vertical conduction, with different boundary conditions. A half-space model involves conductive cooling of a semi-infinite mantle half-space with temperature fixed both along the surface and with depth at the ridge axis (Turcotte & Oxburgh, 1969; Figure 1a). For plate models, the principal difference is that

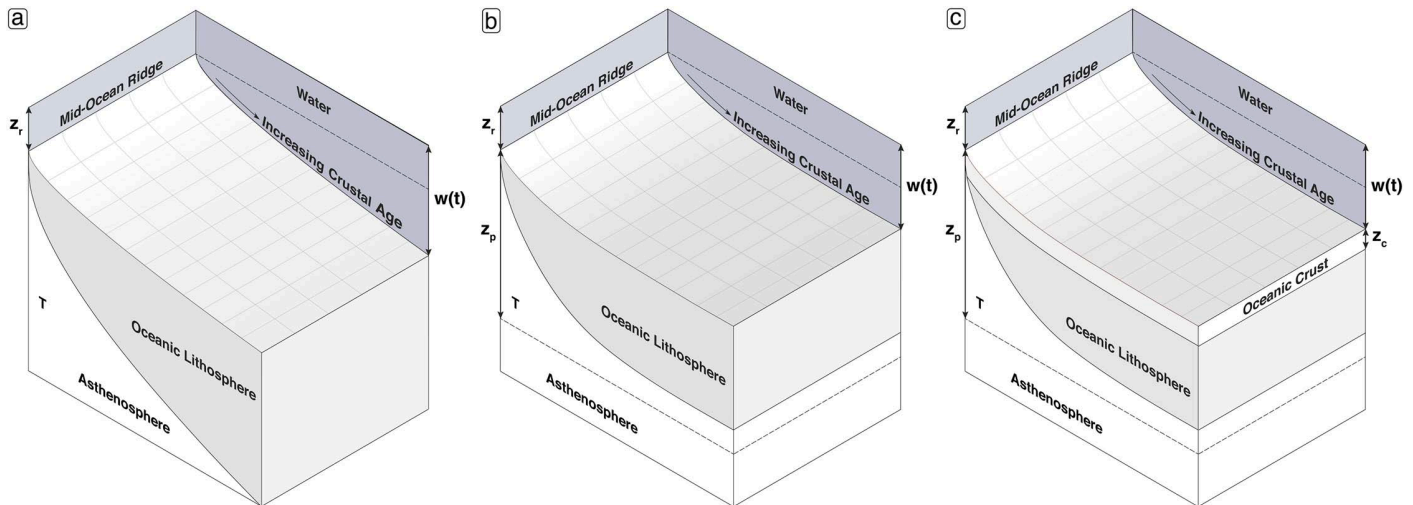


Figure 1. Schematic diagrams of models for the thermal cooling of oceanic lithosphere. (a) Half-space cooling model; $w(t)$ = water depth through time; z_r = water depth at the ridge axis; T = temperature at the ridge axis. (b) Simple plate cooling model; z_p = plate thickness; T = temperature at the ridge axis and basal boundary. (c) Complete plate cooling model; z_c = thickness of oceanic crustal layer; T = mantle potential temperature.

temperature along a basal boundary is also fixed to mimic resupply of heat (McKenzie, 1967; Figure 1b). These calculations yield the temperature distribution within oceanic lithosphere as a function of age.

Turcotte and Oxburgh (1967) used a simple half-space model to argue that age-depth observations from young lithosphere can be accounted for by vertical cooling. Parsons and Sclater (1977) extended age-depth observations for the North Pacific and North Atlantic oceans out to 160 Ma and concluded that these observations are better fitted using a plate as opposed to a half-space model. Using an inverse strategy, they obtained a plate thickness of 125 ± 10 km, a basal and axial temperature of $1350 \pm 275^\circ\text{C}$, and a thermal expansion coefficient of $(3.2 \pm 1.1) \times 10^{-5}\text{K}^{-1}$. This plate model was broadly compatible with existing heat flow observations. Subsequently, Stein and Stein (1992) jointly inverted a revised compilation of age-depth and heat flow observations from the North Pacific and northwest Atlantic oceans to further constrain their plate model. They favored a thinner plate thickness of 95 km, an increased temperature of 1450°C , and a thermal expansion coefficient of $3.1 \times 10^{-5}\text{K}^{-1}$.

The analytical approach that underpins these modeling strategies ignores horizontal conduction of heat and radioactive heat generation, which are thought to be minor in oceanic lithosphere (Jaupart & Mareschal, 2007; McKenzie, 1967). The model also assumes that the thermal conductivity, k , the thermal expansion coefficient, α , and the heat capacity, C_p , of the cooling plate are constant. McKenzie et al. (2005) showed that the thermal structure of a cooling plate can be calculated numerically using experimentally determined values of k , α , and C_p that vary as a function of temperature. They also argued that, if decompression melting yields an oceanic crustal thickness of ~ 7 km, the potential temperature at which the plate forms can be fixed at 1315°C . In their revised plate model, which incorporates an axial melting zone, they match age-depth observations from the north Pacific Ocean (Parsons & Sclater, 1977) and selected heat flow observations (Sclater et al., 1980). Their optimal model has a plate thickness of 106 km and a potential temperature of 1315°C . By including the temperature dependence of k , α , and C_p , McKenzie et al. (2005) predicted that the seismogenic thickness of oceanic lithosphere approximately corresponds to the depth to the 600°C isothermal surface. More recently, increasingly sophisticated plate models that include lithostatic pressure, mineralogic phase transitions, and hydrothermal circulation within oceanic crust have also been developed (Afonso et al., 2007; Grose & Afonso, 2013; Korenaga & Korenaga, 2016; Schmeling et al., 2017; Figure 1c).

Here, our main purpose in revisiting this well-known problem is threefold. First, we summarize and describe a significantly revised and augmented database of global age-depth observations (Hoggard et al., 2017). Our intention is to exploit this database in conjunction with a global inventory of revised heat flow measurements (Hasterok et al., 2011). Second, both databases are jointly inverted using an increasingly complex model to constrain the thermal structure of oceanic lithosphere. Our intention is to identify an optimal model that yields the best fit to the combined age-depth and heat flow databases, while simultaneously

honoring independent constraints for mantle potential temperature, seismologic observations and modern laboratory experiments that constrain the thermal properties of key minerals. Third, we use the resultant thermal structure to reinvestigate rheological properties relating to the seismogenic thickness and depth of the lithosphere-asthenosphere boundary. We also calculate residual topography and predict free-air gravity anomalies throughout the oceanic realm.

2. Observational Databases

2.1. Age-Depth Measurements

An understanding of the thermal evolution of oceanic lithosphere depends upon the availability of a sufficiently accurate and comprehensive database of age-depth measurements. Water-loaded depth to the top of oceanic basement can be accurately determined provided that the thickness and density of both the overlying sedimentary pile and oceanic crust are known. It is important to exclude regions of the oceanic floor where flexural bending occurs (e.g., trenches, seamounts, and plateaux). In the original age-depth compilations exploited by Parsons and Sclater (1977) and Stein and Stein (1992), observations were principally extracted from abundant ship-track records of the North Pacific and North Atlantic oceans. This strategy was later adapted and applied to greater quantities of ship-track records to ensure that regions with significant (but unknown) thicknesses of sediment, with seamounts and plateaux, and with long wavelength free-air gravity anomalies were carefully excluded (e.g., Crosby et al., 2006; Hillier & Watts, 2005; Korenaga & Korenaga, 2008). One disadvantage of this approach is that the resultant compilations end up being mostly restricted to the Pacific plate with a bias toward younger plate ages.

Here we adopt a global strategy that exploits the availability of a burgeoning inventory of seismic reflection surveys acquired and processed by the hydrocarbon industry. In a global analysis, Hoggard et al. (2017) exploited a comprehensive compilation of 1,240 seismic reflection profiles together with 302 modern (i.e., wide angle) and 395 legacy (i.e., refraction) experiments to build a database of water-loaded depths to oceanic basement as a function of plate age (Figure 2a). The quality of this compilation relies on the ability to accurately correct for both sedimentary and crustal loading. Most, but not all, seismic reflection profiles clearly image both the sediment-basement and the Moho interfaces (Figures 2b and 2c). Simple calibration schemes are used to convert the two-way travel time measured for each mapped interface on a seismic reflection profile into the equivalent water-loaded correction (see Hoggard et al., 2017). Sedimentary and crustal corrections are applied to 1,158 spot measurements, each of which has a typical uncertainty of ± 120 m. An additional 870 spot measurements are included that have only been corrected for sedimentary loading. These measurements still provide useful upper or lower bounds. The combined inventory of age-depth measurements has been averaged within 1° bins to yield 2,028 individual values.

Figure 2d shows the resulting water-loaded depth to basement as a function of plate age. We have augmented the age grid of Müller et al. (2016) by including oceanic crust from the Black Sea, the Caspian Sea, and the eastern Mediterranean Sea, as well as the New Caledonian and Aleutian basins. We have also corrected gridding artifacts within the Gulf of California and along the Mohns Ridge using age constraints from Müller et al. (2008). This augmented age grid is provided in the supporting information (Data Set S1). The resultant distribution of age-depth measurements shows that the main control on oceanic bathymetry is subsidence driven by conductive cooling of the lithosphere through time. However, this trend is overprinted by considerable scatter that is thought to be generated by the changing pattern of subplate mantle circulation (Hoggard et al., 2016). In order to exploit this distribution with a view to placing constraints on the thermal evolution of oceanic lithosphere, it is necessary to assume that dynamic topography is approximately evenly distributed as a function of plate age. This assumption is common to most, but not all, studies that use these age-depth measurements. We note that the transient shallowing of basement depth between 90 and 130 Ma observed by Crosby et al. (2006) and attributed by them to a thermal boundary layer instability is not clearly visible in our database. Here we jointly invert this subsidence data with a global inventory of heat flow measurements. A significant advantage of using suites of different observations is that any potential trade-off between model parameters can be mitigated (Stein & Stein, 1992).

2.2. Heat Flow Measurements

Cooling by conductive heat loss through the top of oceanic basement yields an additional valuable constraint for the thermal structure of the oceanic plate since temperature gradients close to the sea floor decrease through time, causing conductive heat flow to decay with plate age. We therefore exploit a global

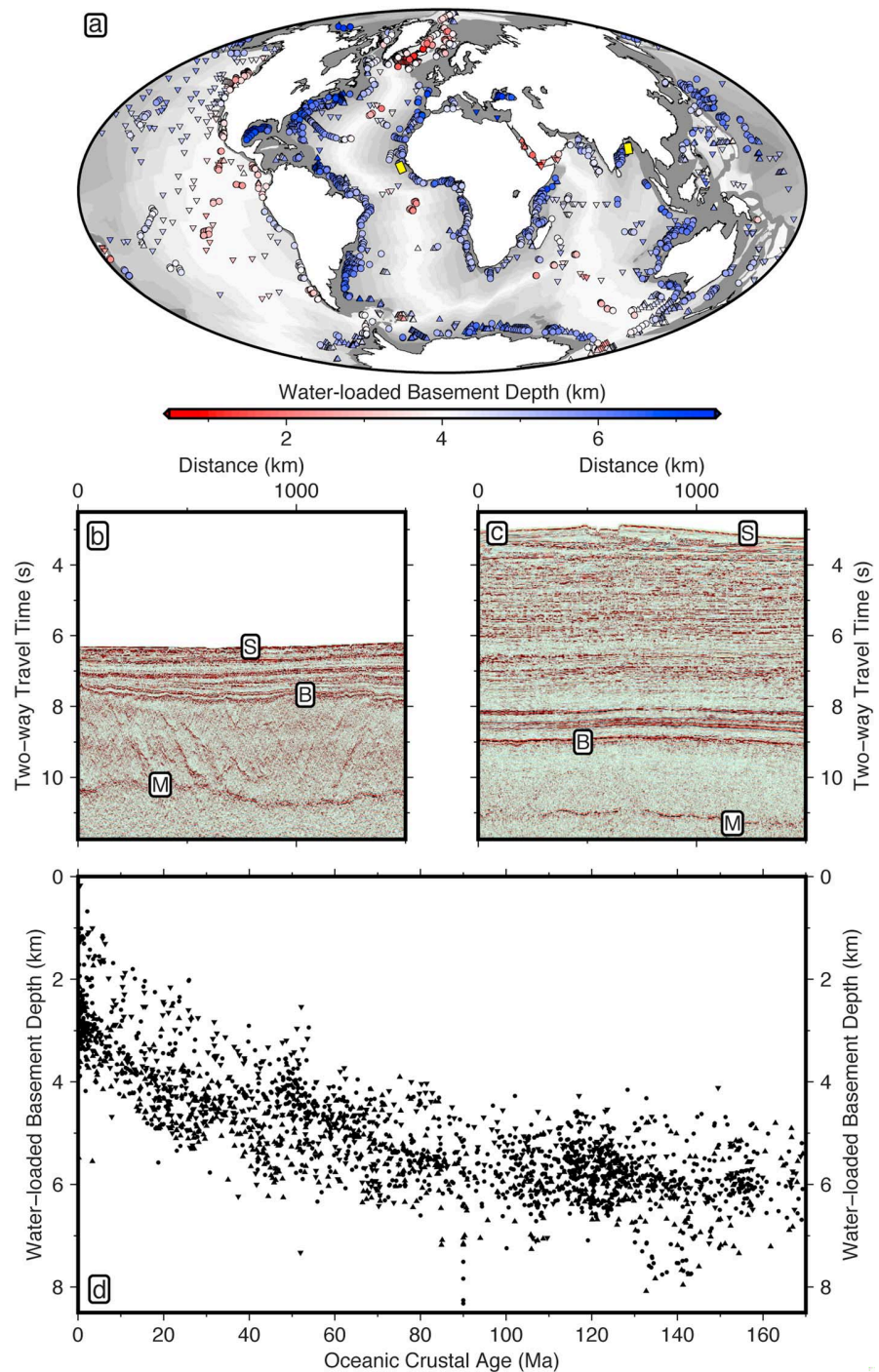


Figure 2. Oceanic age-depth database. (a) Map showing global distribution of 2,028 water-loaded depths to oceanic basement from Hoggard et al. (2017); circles = data with both sedimentary and crustal corrections; upward/downward pointing triangles = lower/upper estimates of depth for which only sedimentary corrections are applied; yellow lines offshore northwest Africa and offshore east India = location of example seismic reflection profiles shown in (b) and (c), respectively; light/dark gray background shading = young/old oceanic plate age. (b) Seismic reflection profile offshore Guinea-Bissau, northwest Africa, courtesy of Spectrum Geo. S = seabed; B = sediment-basement interface; M = Moho (i.e., base of crust). (c) Seismic reflection profile offshore east India, courtesy of ION Geophysical. (d) 2,028 water-loaded depth to oceanic basement plotted as function of plate age.

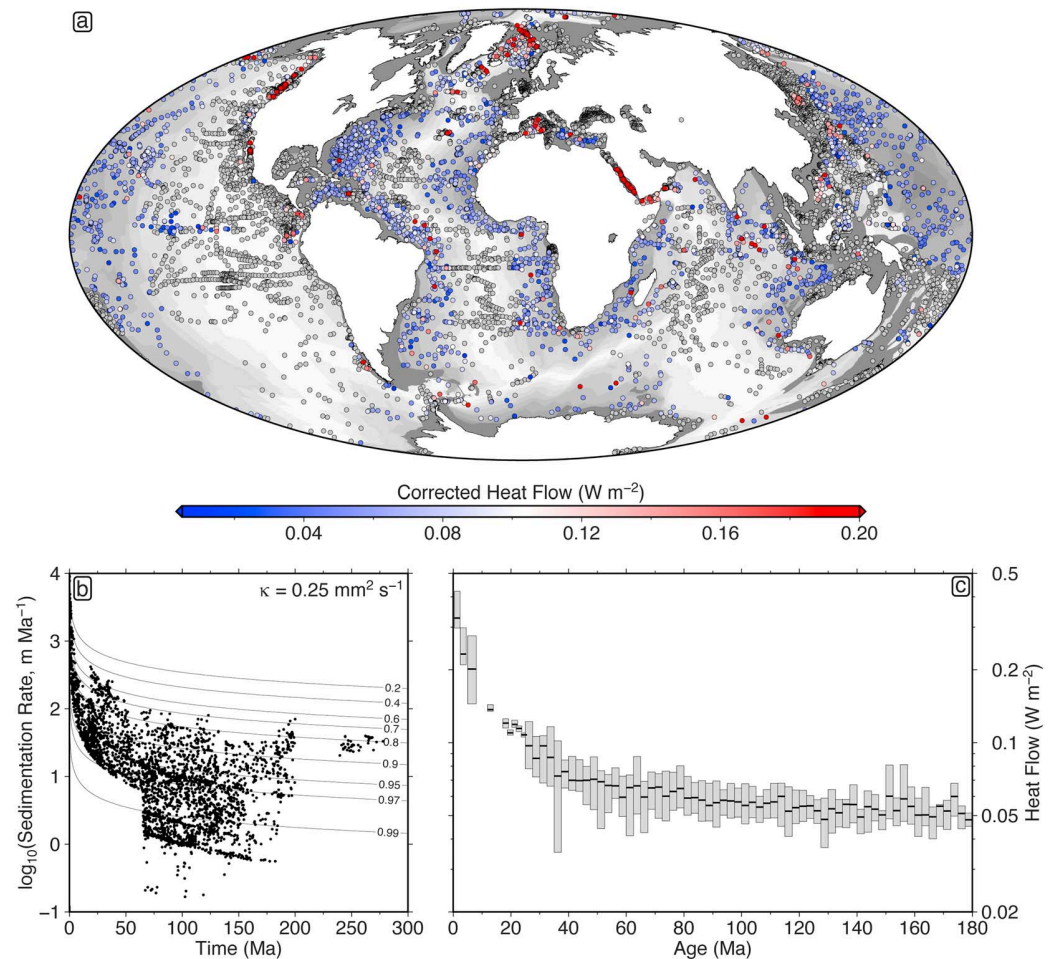


Figure 3. Oceanic heat flow database. (a) Map showing global distribution of heat flow measurements from Hasterok et al. (2011); colored circles = measurements that pass the filtering process; gray circles = measurements removed during filtering process; light/dark gray background shading = young/old oceanic plate age. (b) Sedimentation correction to heat flow measurements from equation (1) using a sedimentary thermal diffusivity of $\kappa = 0.25 \text{ mm}^2 \text{ s}^{-1}$; black circles = heat flow measurements. (c) Corrected surface heat flow binned in 2.5 Myr windows; gray line/box = median and interquartile ranges.

compilation of heat flow measurements that we have corrected in several significant ways (Hasterok et al., 2011). A key advantage of exploiting heat flow measurements is that the long thermal time constant for oceanic lithosphere acts as a buffer against sensitivity to transient temperature perturbations within the underlying asthenospheric mantle. However, the effects of hydrothermal circulation can bias heat flow measurements, especially within younger portions of oceanic lithosphere (Lister, 1972). For this reason, we have paid particular attention to application of a series of corrections.

A global database comprising 23,428 heat flow measurements was assembled by Hasterok et al. (2011) and is shown in Figure 3a. First, we identify those measurements that lie upon oceanic crust as defined by our revised oceanic age grid. We then filtered these heat flow measurements to remove non-positive values and spatially binned the measurements within 0.1° regions, selecting the median value from each bin. This approach reduces the predominance of dense, high-resolution local studies within the global database.

It is desirable to minimize the impact of hydrothermal circulation on the database of heat flow measurements. It has been documented that thin sedimentary cover and the existence of a rugose sediment-basement interface tends to promote hydrothermal circulation (Lister, 1972). Hasterok et al. (2011) describe a set of criteria that are designed to minimize these effects, including removal of measurements where sedimentary thickness is less than 400 m, any that are located within 60 km of a seamount and those which occur on large igneous

provinces. These filters significantly reduce scatter and improve the correlation of heat flow measurements as a function of plate age. We apply identical filters to measurements from oceanic crust that is younger than 65 Ma. Sedimentary thicknesses are extracted from the NGDC_v2 grid (Whittaker et al., 2013). Where appropriate, we have infilled regions with no measurements by exploiting values from the CRUST1.0 compilation (Laske et al., 2013). The seamount inventory is taken from Wessel et al. (2010) and the distribution of large igneous provinces is from Coffin and Eldholm (1994). Note that we do not cull any measurements by using theoretical cooling models in order to sidestep potential circularity (*contra* Hasterok et al., 2011). Significantly, a consequence of our initial spatial binning is that no individual measurements have values $> 500 \text{ mW m}^{-2}$ above the running mean.

These hydrothermal filtering criteria have not been applied to measurements from oceanic crust older than 65 Ma since hydrothermal circulation is thought to be negligible for older ages (Hasterok, 2013; Stein & Stein, 1992). Should these filtering criteria be applied to measurements older than 65 Ma data, fewer measurements are selected, which leads to a slight increase in interquartile ranges and to greater scatter between age bins. However, the resultant median heat flow values do not systematically change, which is consistent with the expectation of limited hydrothermal circulation at older ages. For this reason, we have chosen to keep all heat flow measurements from oceanic crust older than 65 Ma.

The rate at which sediment is deposited on the seabed can affect heat flow measurements. Since sediment has an initial temperature that is equal to bottom water, deposition acts to depress the geothermal profile, leading to an underestimate of heat flow. An analytical solution that describes the magnitude of this effect is provided by Von Herzen and Uyeda (1963), who assumed that sedimentation rate and thermal diffusivity are constant as a function of time and that the effects of sedimentary compaction and hydrothermal circulation are negligible. In the absence of internal heat generation, their expression is simplified to give the fractional disturbance, F , of the geothermal profile at the seabed

$$F = 1 + 2Y^2 \text{erfc}(Y) - \text{erf}(Y) - \frac{2Y}{\sqrt{\pi}} \exp(-Y^2), \quad (1)$$

where $Y = \frac{1}{2} U t^{\frac{1}{2}} \kappa^{-\frac{1}{2}}$, U is a constant sedimentation rate, t is time since onset of sedimentation, and κ is thermal diffusivity. Following Hasterok et al. (2011), we estimate the value of U by dividing the total sedimentary thickness by plate age. For a thermal diffusivity of $0.25 \text{ mm}^2 \text{ s}^{-1}$, 60% of the remaining measurements within the heat flow database require a sedimentary correction of less than 5% and 91% are corrected by $< 20\%$ (Figure 3b). Measurements requiring significant correction occur either on young oceanic crust or on crust with large sedimentation rates such as major deltas and sedimentary basins surrounded by elevated continental lithosphere. Measurements from the Caspian, Gulf of Mexico, and Black seas are discarded due to significant post-Miocene increases in clastic flux in these regions, which violate the assumption of constant sedimentation rate (Galloway et al., 2011; Guliyev et al., 2003; Simmons et al., 2018). This procedure leaves 3,597 corrected heat flow measurements, which are then binned into 2.5 Myr windows. Discarding any measurements that require sedimentation corrections of greater than either 20% or 5% does not significantly alter heat flow statistics for ages $\geq 40 \text{ Ma}$, although variability does increase for younger age bins.

We have also tested the effect of using a range of thermal diffusivity values for sediment that vary between 0.1 and $0.5 \text{ mm}^2 \text{ s}^{-1}$, which encompass the values typically encountered for carbonaceous sediments (Waples & Waples, 2004). Reducing diffusivity values gives rise to greater variation of geothermal profiles and larger sedimentary corrections. However, a value of $\kappa = 0.1 \text{ mm}^2 \text{ s}^{-1}$ increases median heat flow values by less than 3% at young ages and has an even smaller effect on older bins. A value of $\kappa = 0.5 \text{ mm}^2 \text{ s}^{-1}$ systematically reduces the median heat flow within each bin by $< 2\%$ for ages greater than 15 Ma. These minor adjustments are significantly smaller than the interquartile range for each bin, which suggests that uncertainty in the value of sedimentary thermal diffusivity has a relatively minor impact on resultant heat flow values.

Heat flow statistics show that elevated values of $> 180 \text{ mW m}^{-2}$ occur for young plate ages, decreasing to $100 \pm 20 \text{ mW m}^{-2}$ by 20 Ma. At 60 Ma, heat flow measurements are $65 \pm 15 \text{ mW m}^{-2}$ and steadily decrease to $50 \pm 8 \text{ mW m}^{-2}$ for ages $> 125 \text{ Ma}$. It has been suggested that, despite global filtering of measurements to limit the effects of hydrothermal circulation, there still exists a significant hydrothermal deficit for plate ages of $< 25 \text{ Ma}$ (Hasterok, 2013). A handful of detailed studies have been carried out at specific locations on young oceanic crust where there is a dense coverage of both heat flow and seismic reflection surveys (Hasterok et al., 2011). Compared with the results of these studies, our corrected and binned database may systematically

underpredict actual heat flow measurements by 25–40% within this age range. Hasterok (2013) suggests that average heat flow values for ages < 25 Ma should instead be taken from these specific sites, despite increased spatial bias. Following this approach, we adopt these values for < 25 Ma lithosphere and use our global compilation for older age bins (Figure 3c).

3. Modeling Strategy

Following adiabatic upwelling beneath a mid-ocean ridge, mantle material is transported laterally at a rate governed by plate spreading. This material progressively cools as it moves further away from the ridge. Provided that the half-spreading rate exceeds $\sim 10 \text{ mm a}^{-1}$, the horizontal component of heat conduction can be regarded as negligible (McKenzie et al., 2005). Furthermore, heat generation by radioactive decay only makes a minor contribution within oceanic lithosphere. Pioneering models of the thermal evolution of oceanic lithosphere assume constant values of physical parameters that govern thermal evolution (Jaupart & Mareschal, 2007). The most important parameters are thermal conductivity, k , thermal expansivity, α , and isobaric specific heat capacity, C_p (Parsons & Sclater, 1977; Stein & Stein, 1992; Turcotte & Oxburgh, 1967; Turcotte & Schubert, 2002). Despite the success of thermal models that assume constant values of these parameters, McKenzie et al. (2005) re-examined this approach by taking into account their temperature dependence. Laboratory studies show that k , α , and C_p vary significantly over temperature and pressure ranges that are deemed appropriate to the upper mantle (Berman & Aranovich, 1996; Bouhifd et al., 1996; Hofmeister & Pertermann, 2008). McKenzie et al. (2005) also included the effects of adiabatic decompression melting at the ridge axis, while Grose and Afonso (2013) and Korenaga and Korenaga (2016) included differences in the thermal properties of oceanic crust and mantle.

Cooling oceanic lithosphere is advected horizontally from the ridge axis at a fixed velocity and the evolution of its temperature structure depends only upon age for plate velocities $\geq 10 \text{ mm a}^{-1}$. The evolving thermal structure is calculated using a generalized form of the one-dimensional heat equation in a reference frame that translates horizontally with the spreading lithosphere

$$\frac{\partial [\rho(T, P, X)C_p(T, X)T]}{\partial t} = \frac{\partial}{\partial z} \left[k(T, P, X) \frac{\partial T}{\partial z} \right] \quad (2)$$

where t is time; z is depth; ρ is density; and T , P , and X refer to temperature, pressure and composition. In this equation, k and ρ vary as functions of T , P , and X , whereas C_p depends only upon temperature and composition, since pressure dependence of this parameter is negligible over the relevant pressure range (Hofmeister, 2007). Although simple analytical solutions exist for the half-space and plate models if thermal parameters are constant, equation (2) must be solved numerically if thermal parameters vary as a function of temperature, pressure, and composition (McKenzie et al., 2005; Turcotte & Schubert, 2002). Here we explore the applicability of the half-space cooling and plate models, but we do not investigate the constant heat flow model of Doin and Fleitout (1996) since it requires the existence of steep temperature gradients at the base of the cooling plate close to the ridge axis. This requirement is incompatible with the expected axial temperature profile, which is dominantly controlled by adiabatic decompression and melting.

Following McKenzie et al. (2005), if an expression for the integral

$$G = \int k(T) dT \quad (3)$$

can be found, then equation (2) can be reformulated as

$$\frac{\partial T}{\partial t} = \frac{1}{\rho C_p} \frac{\partial^2 G}{\partial z^2} - \frac{T}{\rho C_p} \frac{\partial(\rho C_p)}{\partial t} \quad (4)$$

where the second term on the right-hand side is considerably smaller than the first. We solve equation (4) numerically using an unconditionally stable time- and space-centered Crank-Nicholson finite-difference scheme with a predictor-corrector step (Press et al., 1992). Accordingly, equation (4) is recast as

$$\begin{aligned} T_j^{n+1} + A \left[-\frac{k_{j+\frac{1}{2}}^m}{\Delta z_j^m} T_{j+1}^{n+1} + \left(\frac{k_{j+\frac{1}{2}}^m}{\Delta z_j^m} + \frac{k_{j-\frac{1}{2}}^m}{\Delta z_{j-1}^m} \right) T_j^{n+1} - \frac{k_{j-\frac{1}{2}}^m}{\Delta z_{j-1}^m} T_{j-1}^{n+1} \right] \\ = T_j^n + A \left[\frac{k_{j+\frac{1}{2}}^m}{\Delta z_j^m} T_{j+1}^n - \left(\frac{k_{j+\frac{1}{2}}^m}{\Delta z_j^m} + \frac{k_{j-\frac{1}{2}}^m}{\Delta z_{j-1}^m} \right) T_j^n + \frac{k_{j-\frac{1}{2}}^m}{\Delta z_{j-1}^m} T_{j-1}^n \right] + B \end{aligned} \quad (5)$$

Table 1
Results for Joint Fitting of Subsidence and Heat Flow Databases

Model	z_c (km)	T -dependence	P -dependence	T (°C)	χ_t	$[\chi_t]_{1333^\circ\text{C}}$	z_r (m)	$[z_r]_{1333^\circ\text{C}}$ (m)	z_p (km)	$[z_p]_{1333^\circ\text{C}}$ (km)	Q (TW)	$[Q]_{1333^\circ\text{C}}$ (TW)
HSCk	0	None	None	1484	0.898	1.094	1656	2000	—	—	28.76	25.83
Pk	0	None	None	1495	0.750	0.976	2216	2808	105	88	32.72	30.28
MR*	0	MJP05	None	1409	0.731	0.754	2512	2636	95	92	28.74	27.88
KR	0	KK16 & GA13	None	1106	0.750	1.214	2568	< 2000	120	124	29.01	32.72
KRC	0	KK16 & GA13	GA13	1102	0.744	1.291	2640	2040	140	146	28.97	33.78
KRCCK	7	KK16 & GA13	GA13	1308	0.728	0.732	2712	2652	137	137	27.08	27.45
KRCC	7	KK16 & GA13	GA13	1302	0.726	0.733	2636	2572	136	138	27.49	27.95

Note. Model characterizations and optimal parameters where T is either a free parameter or fixed at 1333°C (labelled with $[X]_{1333^\circ\text{C}}$ subscripts). HSCk = half-space cooling model (Figure 4); Pk = simple plate model (Figure 5); MR* = temperature-dependent plate model following McKenzie et al. (2005; Figure 6); KR = temperature-dependent plate model using updated olivine conductivity (Figure S1); KRC = compressible temperature- and pressure-dependent plate model using updated olivine conductivity (Figure S2); KRCCK = complete plate model with constant conductivity crustal layer; KRCC = complete plate model with temperature- and pressure-dependent conductivity in crustal layer (Figure 8). z_c = crustal thickness; T - and P -dependence columns show parameterizations used for each model: MJP05 = parameters from McKenzie et al. (2005), GA13 = Grose and Afonso (2013) and KK16 = Korenaga and Korenaga (2016); T = optimal mantle temperature; z_p = optimal plate thickness; z_r = optimal zero-age ridge depth; χ_t = value of combined misfit; Q = predicted integrated oceanic heat flow.

where

$$A = \frac{\Delta t}{\rho_j^m C_{pj}^m (\Delta z_j^m + \Delta z_{j-1}^m)} \quad (6)$$

For the predictor step $m = n$, while for the corrector step $m = n + \frac{1}{2}$. B is included as a correction that represents the second term on the right-hand side of equation (4). For the predictor step we use

$$B = - \frac{T_j^n (\rho_j^n C_{pj}^n - \rho_j^{n-1} C_{pj}^{n-1})}{\rho_j^n C_{pj}^n} \quad (7)$$

and for the corrector step we employ

$$B = - \frac{(T_j^{n+1} + T_j^n) (\rho_j^{n+1} C_{pj}^{n+1} - \rho_j^n C_{pj}^n)}{\rho_j^{n+1} C_{pj}^{n+1} + \rho_j^n C_{pj}^n} \quad (8)$$

This set of equations is solved by tridiagonal elimination (Press et al., 1992). For incompressible models, Δz_j^m has a constant value of 1 km, while in compressible models, Δz_j^m is space-centered and scales with thermal contraction. We use a timestep $\Delta t = 5$ kyr, and the maximum magnitude of the corrector step is initially $\sim 4^\circ\text{C}$, dropping to 0.1°C by 1.4 Ma, reducing to $< 0.01^\circ\text{C}$ by 18 Ma. A suite of half-space and plate models using both constant and variable thermal parameters have been analyzed and compared with age-depth and heat flow observations. A summary of these models is provided in Table 1.

The analytical half-space and plate models must have a constant temperature, T , assigned to the ridge axis and ridge axis/basal boundary, respectively. The numerical models with non-constant parameters can use a more realistic temperature structure for these boundaries. In these models, we select a potential temperature, T , which is combined with a plate thickness and adiabatic gradient to calculate the absolute temperature along the basal boundary. The initial ridge axis temperature profile is calculated using this same adiabatic gradient except when it intersects the solidus for anhydrous lherzolite and undergoes decompression melting (Katz et al., 2003). The geothermal gradient above this depth is calculated using the melting parameterization of Shorttle et al. (2014), which yields crustal thicknesses of 0.01–41.10 km for the potential temperature range 1100–1650°C. Temperature is assumed to linearly decrease from the melting parameterization value at 7 km depth to 0°C at the surface. Realistic changes to the detailed shape of this initial temperature profile have a negligible effect on inferred optimal values of potential temperature, plate thickness, and depth of ridge axis.

Thermal models that predict the development of oceanic lithosphere must be consistent with independent constraints on axial temperature structure derived from either the thickness of oceanic crust or the geochemistry of mid-ocean ridge basalts (McKenzie et al., 2005). Global compilations of marine seismic experiments yield an average crustal thickness of 6.9 ± 2.2 km (Hoggard et al., 2017; White et al., 1992). Within our melting parameterization, this range of thickness is produced when the potential temperature is $1331 \pm 35^\circ\text{C}$.

If the mantle is hydrated by 113 ppm, for example, the inferred potential temperature would decrease by $\sim 11^\circ\text{C}$ (Brown & Leshner, 2016). We note that this inferred potential temperature is also dependent upon globally averaged modal proportions of fertile pyroxenite, lherzolite and harzburgite within the melting region. These proportions are poorly constrained, but if the mass fraction of fertile pyroxenite was up to $\sim 5\%_{\text{px}}$, the inferred potential temperature decreases by $\sim 6^\circ\text{C } \%_{\text{px}}^{-1}$ (Shorttle et al., 2014). An alternative suite of constraints comes from analyses of mid-ocean ridge basalt geochemistry. A variety of petrologic and geochemical studies yield similar estimates for ambient mantle potential temperatures (e.g., $1250\text{--}1350^\circ\text{C}$: Katsura et al., 2004; $1280\text{--}1400^\circ\text{C}$: Herzberg et al., 2007; $1314\text{--}1464^\circ\text{C}$: Dalton et al., 2014; $1318^{+44}_{-32}^\circ\text{C}$: Matthews et al., 2016). Geochemical and geophysical arguments are therefore in reasonable agreement for ambient potential temperatures of $T = 1340 \pm 60^\circ\text{C}$.

4. Age-Depth and Heat Flow Calculations

For the half-space cooling model with constant thermal parameters, plate subsidence, w , as a function of time, t , is calculated analytically using

$$w(t) = z_r + \frac{2\rho_m\alpha(T - T_0)}{\rho_m - \rho_w} \sqrt{\frac{\kappa t}{\pi}} \quad (9)$$

where z_r is water depth at the ridge axis, $\rho_m = 3.33 \text{ Mg m}^{-3}$ is the density of mantle at 0°C , $\rho_w = 1.03 \text{ Mg m}^{-3}$ is the density of seawater, $\alpha = 3.28 \times 10^{-5} \text{ K}^{-1}$ is the thermal expansion coefficient, T is the temperature of the ridge axis, $T_0 = 0^\circ\text{C}$ is surface temperature and $\kappa = k/(\rho_m C_p) = 0.8044 \text{ mm}^2 \text{ s}^{-1}$ is thermal diffusivity. For a simple analytical plate model with constant thermal parameters, w is calculated using

$$w(t) = z_r + \frac{\rho_m\alpha(T - T_0)z_p}{2(\rho_m - \rho_w)} \left[1 - \frac{8}{\pi^2} \sum_{i=0}^N \frac{1}{(1 + 2i)^2} \exp\left(-\frac{\kappa(1 + 2i)^2\pi^2 t}{z_p^2}\right) \right] \quad (10)$$

where z_p is equilibrium plate thickness, T is temperature at the ridge axis and basal boundary and i is an integer whose maximum value $N = 100$ is chosen to ensure appropriate convergence. For incompressible plate models that include temperature-dependent parameters, we use

$$w(t) = z_r + \frac{1}{\rho_m - \rho_w} \left[\int_0^{z_p} \rho(0, z) dz - \int_0^{z_p} \rho(t, z) dz \right]. \quad (11)$$

For compressible plate models that include both temperature- and pressure-dependent parameters, we use

$$w(t) = z_r + \frac{\rho_b}{\rho_b - \rho_w(t)} \int_0^{z_p} \left[1 - \frac{\rho(0, z')}{\rho(t, z')} \right] dz' \quad (12)$$

where z' is the Lagrangian depth coordinate that contracts vertically with compression, ρ_b is the density at the depth of compensation (i.e., the shallowest depth where $\rho(t, z')$ and $\rho(0, z')$ are equal) and $\rho_w(t) = 1.028 + 0.0048w(t) \text{ Mg m}^{-3}$ (with $w(t)$ in km) in order to account for the compressibility of seawater (Grose & Afonso, 2013).

For the half-space cooling model, surface heat flow, H , is analytically calculated using

$$H(t) = \frac{k(T - T_0)}{\sqrt{\pi\kappa t}} \quad (13)$$

where $k = 3.138 \text{ W m}^{-1} \text{ K}^{-1}$ is the thermal conductivity. For a simple plate model with constant thermal parameters, H is given by

$$H(t) = \frac{k(T - T_0)}{z_p} \left[1 + 2 \sum_{i=1}^N \exp\left(-\frac{\kappa i^2 \pi^2 t}{z_p^2}\right) \right] \quad (14)$$

For all numerical models, surface heat flow is determined using

$$H(n\Delta t) = \frac{k_0^n (T_1^n - T_0^n)}{\Delta z_0^n} \quad (15)$$

where n is the time step of magnitude Δt , k_0^n is the surface conductivity and Δz_0 is the depth increment at the surface.

To minimize the misfit between observed and calculated subsidence, we have chosen a trial function

$$\chi_s = \sqrt{\frac{1}{M} \sum_{i=1}^M \left(\frac{w_i^o - w_i^c}{\sigma_i} \right)^2} \quad (16)$$

where w_i^o and w_i^c are observed and calculated values of water-loaded subsidence, σ_i is the standard deviation of observed subsidence (~ 700 m), and $M = 2028$ is the number of measurements. We have not binned these subsidence observations since any uneven age distribution could give rise to an unintended bias toward regions with large positive or negative residual depth anomalies. Subsidence observations from seafloor that is younger than 5 Ma are excluded in order to sidestep any possible effects of hydrothermal circulation near the ridge axis.

The misfit between observed and calculated heat flow is minimized using a similar trial function given by

$$\chi_h = \sqrt{\frac{1}{M} \sum_{i=1}^M \left(\frac{H_i^o - H_i^c}{\sigma_i^*} \right)^2} \quad (17)$$

where H_i^o and H_i^c are observed and calculated values of heat flow and σ_i^* is defined as the interquartile range of each bin divided by 1.349, in accordance with the statistical analysis of Hasterok (2013). As before, observations from seafloor that is younger than 5 Ma are excluded. We have also excised observations from seafloor older than 168 Ma due to noisier measurements arising from increasing spatial bias. These two misfit functions are equally weighted and combined into a single misfit function given by

$$\chi_t = \sqrt{\frac{\chi_s^2 + \chi_h^2}{2}}. \quad (18)$$

For the half-space cooling model there are two adjustable parameters: water depth at the ridge axis, z_r , and axial temperature, T . A simple analytical plate model has three adjustable parameters: z_r , the plate thickness, z_p , and the temperature of the basal boundary and ridge axis, T . For more complex plate models, T is now mantle potential temperature. Given the small number of dimensions, the misfit space is easily interrogated using parameter sweeps, which enables the shape of the misfit function to be determined and the global minimum identified. In such sweeps, T is typically varied between 1100 and 1600°C at intervals of 25°C, z_r is varied between 1.5 and 3 km at intervals of 0.05 km, and z_p is varied between 50 and 210 km at intervals of 5 km.

5. Model Assessment

Our principal aim is to use revised databases of basement subsidence and heat flow to identify a thermal model which best represents the average behavior of oceanic lithosphere. The optimal model should have several qualities. First, it should have the ability to jointly fit subsidence and heat flow observations. Second, it should predict a temperature that agrees with independent geochemical and petrologic constraints. Finally, it should be the simplest physical model that is consistent with both experimental data on the thermal properties of minerals and a range of additional observations such as earthquake hypocentral depths and lithospheric thickness measurements.

5.1. Half-Space Cooling Models

In its simplest form, this model yields an excellent fit between observed and calculated subsidence as a function of time (Figure 4a). Unfortunately, Figure 4c shows that this fit is predicated upon a temperature of $T = 1005^\circ\text{C}$, which is considerably lower than that determined by petrologic observations (i.e., $1340 \pm 60^\circ\text{C}$). Although there is a negative trade-off between T and z_r , it is evident that T cannot be increased by the required amount of about 300°C without both an unreasonably large decrease in z_r and a significant increase in χ_s .

If subsidence and heat flow measurements are jointly fitted, the half-space cooling model tends to overpredict subsidence and to underpredict heat flow for plate ages greater than ~ 80 Ma (Figures 4a and 4b). Furthermore, Figure 4e shows that the optimal value of $T = 1484^\circ\text{C}$ is almost 100°C greater than the upper bound of independent constraints. The failure to reproduce the observed flattening of heat flow and subsidence for older plates, and the mismatch to independent axial temperature constraints, demonstrates that half-space cooling models do not represent an adequate approximation of the average thermal structure of oceanic lithosphere.

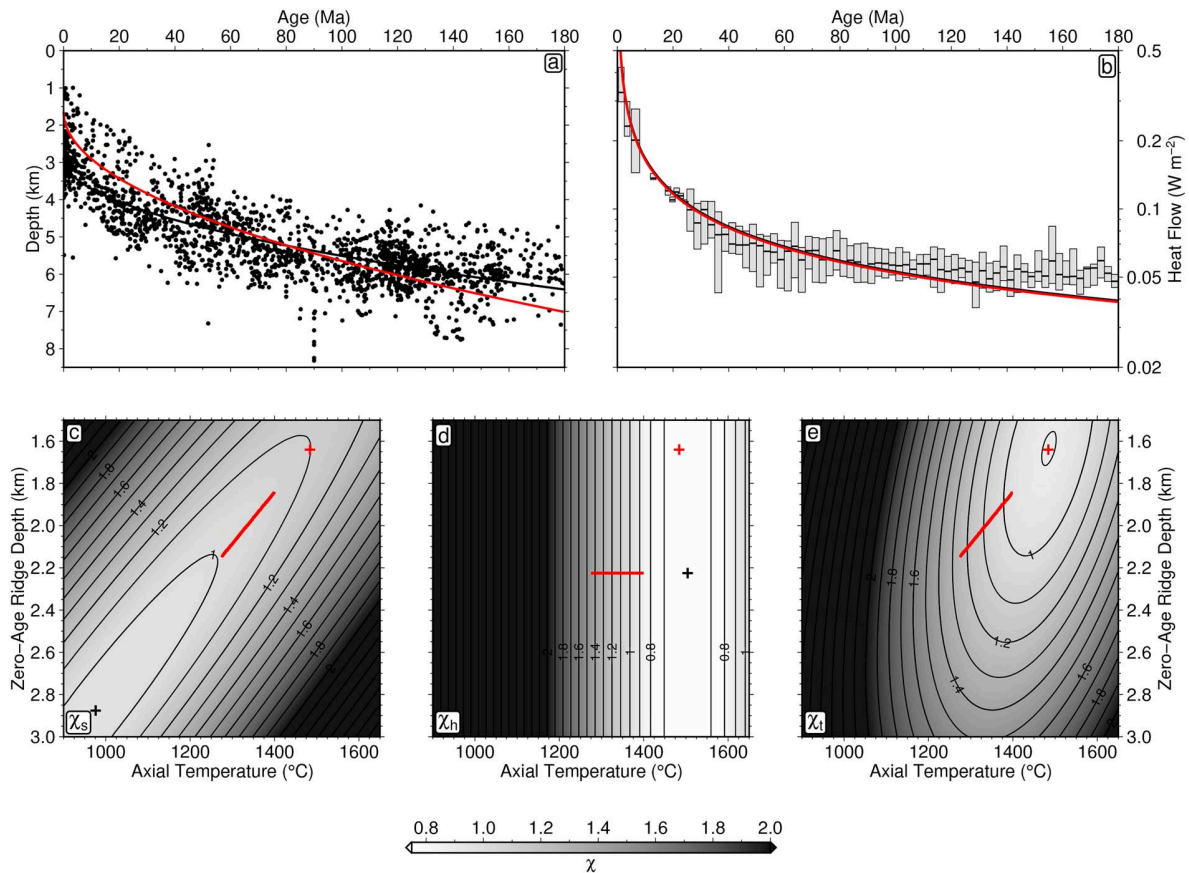


Figure 4. Half-space cooling model. (a) Water-loaded depth to oceanic basement as function of plate age (Figure 2d); black line = optimal relationship obtained by only fitting age-depth observations; red line = optimal relationship from joint fit of age-depth and heat flow observations. (b) Surface heat flow as function of plate age (Figure 3c); gray boxes with horizontal bars = interquartile ranges of sediment-corrected heat flow measurements and median values; black line = optimal relationship obtained by only fitting heat flow observations; red line = optimal relationship from joint fit of age-depth and heat flow observations. (c) Misfit between observed and calculated age-depth observations, χ_s , as function of axial temperature and zero-age ridge depth; black cross = misfit minimum; red bar = optimal parameters when axial temperature is fixed at $1340 \pm 60^{\circ}C$. (d) Same for misfit between observed and calculated heat flow, χ_h . (e) Same for joint misfit, χ_t , between observed and calculated age-depth and heat flow observations; red cross = global minimum used to generate red curves in panels (a) and (b).

5.2. Plate Models

It has previously been argued that a simple analytical plate model provides an adequate fit to combined subsidence and heat flow observations (Parsons & Sclater, 1977; Stein & Stein, 1992). Here we show that the revised databases of both sets of observations can be accurately fitted with a joint residual misfit of $\chi_t \sim 0.8$ (Figure 5). A global minimum occurs at $T = 1495^{\circ}C$, $z_p = 105$ km and $z_r = 2.22$ km (Figure 5e). Notably, if we repeat the approach of Parsons and Sclater (1977) by only fitting subsidence data, we recover a minimum misfit at $T = 1307^{\circ}C$ and $z_p = 129$ km, which is consistent with their original result of $T = 1350 \pm 275^{\circ}C$ and $z_p = 125 \pm 10$ km (Figure 5c). In comparison, our results for matching the combined subsidence and heat flow closely agree with those of Stein and Stein (1992) who retrieve a hotter and thinner plate with $T = 1450^{\circ}C$ and $z_p = 90$ km in their joint-fitting approach (Figure 5e).

It is evident that a simple plate model yields an improved fit to the combined database of subsidence and heat flow observations compared with the half-space model (Figure 5 and Table 1). However, a recovered temperature of $T = 1495^{\circ}C$ is significantly hotter than the independently determined value of $1340 \pm 60^{\circ}C$. A predicted zero-age ridge depth of $z_r = 2.22$ km is also markedly shallower than the global average of $\sim 2.85 \pm 0.5$ km (Gale et al., 2014). Crucially, there is a substantial mismatch in optimal parameters required by subsidence data compared to heat flow observations (Figures 5c and 5d). Thus the shape of the combined misfit function offers little room for manoeuvre in terms of trade-off between plate thickness and temperature (Figure 5e). These discrepancies imply that despite the apparent success of the simple plate model, a more complex approach is required.

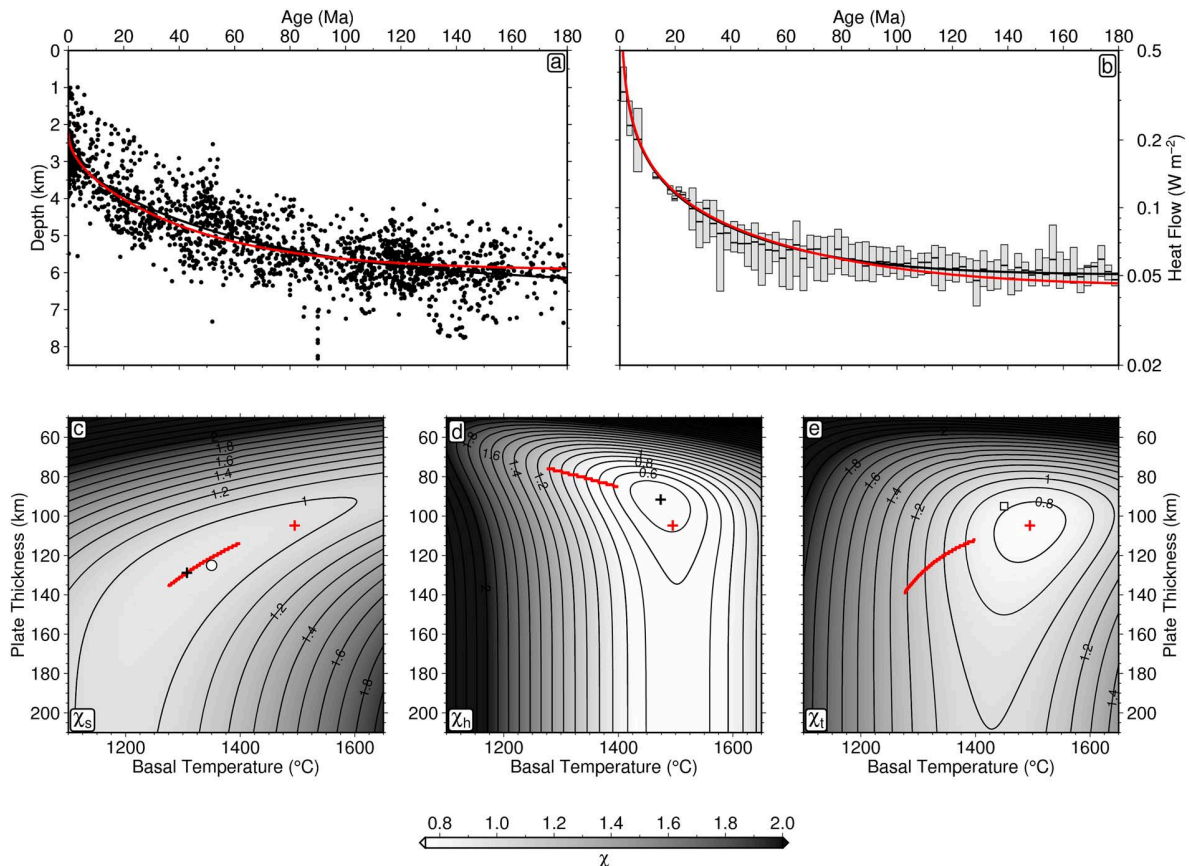


Figure 5. Simple plate model with constant thermal parameters. (a) Water-loaded depth to oceanic basement as function of plate age (Figure 2d); black line = optimal relationship obtained by only fitting age-depth observations; red line = optimal relationship from joint fit of age-depth and heat flow observations. (b) Surface heat flow as function of plate age (Figure 3c); gray boxes with horizontal bars = interquartile ranges of sediment-corrected heat flow measurements and median values; black line = optimal relationship obtained by only fitting heat flow observations; red line = optimal relationship from joint fit of age-depth and heat flow observations. (c) Misfit between observed and calculated age-depth observations, χ_s , as function of basal temperature and plate thickness, sliced at best fitting zero-age depth of 2.35 km; black cross = misfit minimum; red bar = optimal parameters when basal temperature is fixed at $1340 \pm 60^\circ\text{C}$; white circle = optimal result of Parsons and Sclater (1977). (d) Same for misfit between observed and calculated heat flow, χ_h . (e) Same for joint misfit, χ_t , between observed and calculated age-depth and heat flow observations, sliced at best fitting zero-age depth of 2.20 km; red cross = global minimum used to generate red curves in panels (a) and (b); white square = optimal result of Stein and Stein (1992).

5.2.1. Temperature- and Pressure-Dependent Parameterizations

Here we follow the approach described by McKenzie et al. (2005) who propose and apply a more physically realistic parameterization of conductivity, k , expansivity, α , and heat capacity, C_p , within the framework of a plate model. In the first instance, we adopt and benchmark against their temperature-dependent approach and excellent individual fits to either subsidence or heat flow observations are generated (Figures 6a and 6b). The shape of the joint misfit function indicates that there is a global minimum at $T = 1409^\circ\text{C}$, $z_p = 95$ km, and $z_r = 2.51$ km (Figure 6e). This result is $\sim 85^\circ\text{C}$ cooler than obtained for a simple plate model, but it is hotter and thinner than that calculated by McKenzie et al. (2005) who independently fixed $T = 1315^\circ\text{C}$ and $z_r = 2.5$ km to obtain an equilibrium plate thickness of $z_p = 106$ km. Thus, there remains a significant discrepancy between retrieved values of T and z_p compared with those expected from petrologic and seismologic constraints (Burgos et al., 2014; Herzberg et al., 2007; Steinberger & Becker, 2016).

Laboratory-based results, upon which the temperature dependence of conductivity, thermal expansivity, and isobaric heat capacity are based, have associated uncertainties (Figures 7a, 7c, and 7e). We have examined the sensitivity of our results to these uncertainties by carrying out a series of misfit function sweeps for temperature, plate thickness and zero-age ridge depth using parameterizations that are fitted to either upper or lower bounds of the experimental data sets. For example, heat capacity was varied by altering the forsterite-fayalite ratio in accordance with the expected range within the mantle (i.e., $\text{Fo}_{84}\text{--Fo}_{92}$). This variation produces a

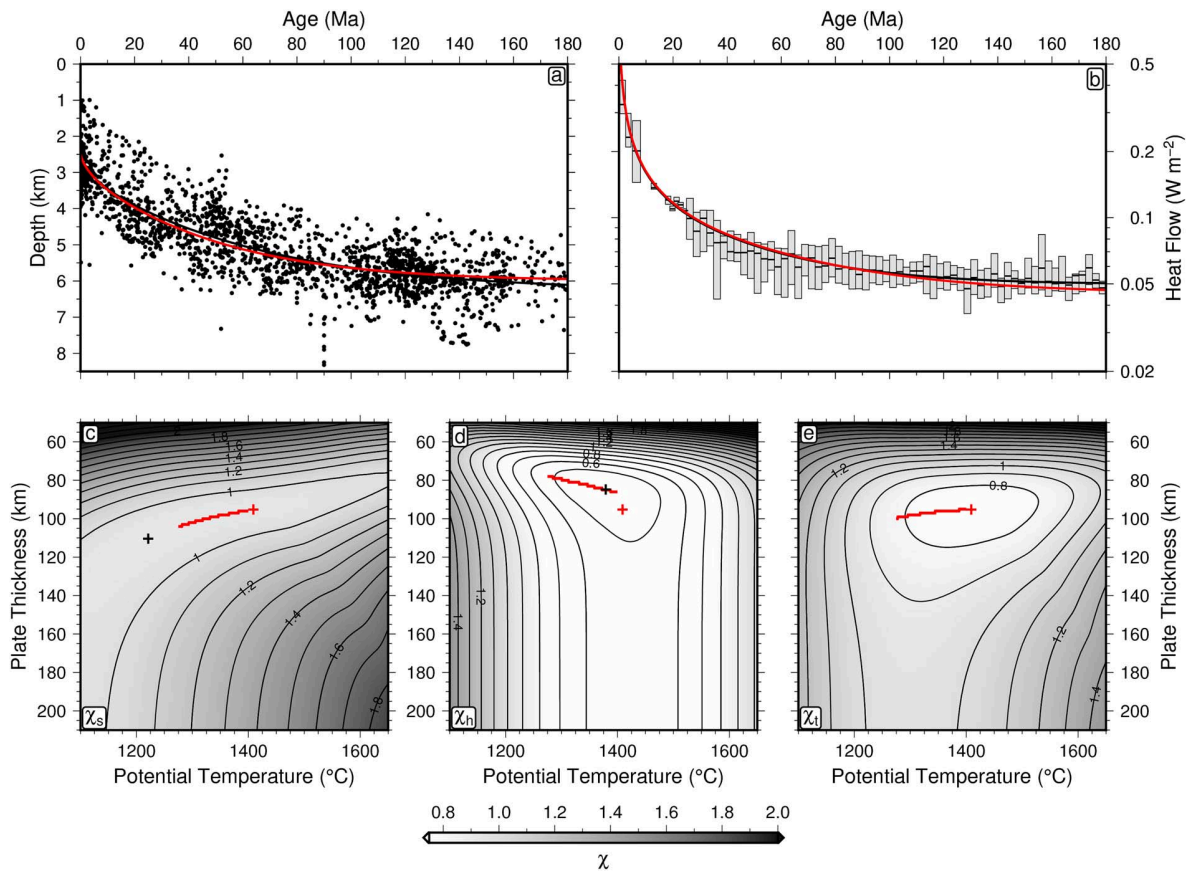


Figure 6. Temperature-dependent plate model. (a) Water-loaded depth to oceanic basement as function of plate age (Figure 2d); black line = optimal relationship obtained by only fitting age-depth observations; red line = optimal relationship from joint fit of age-depth and heat flow observations. (b) Surface heat flow as function of plate age (Figure 3c); gray boxes with horizontal bars = interquartile ranges of sediment-corrected heat flow measurements and median values; black line = optimal relationship obtained by only fitting heat flow observations; red line = optimal relationship from joint fit of age-depth and heat flow observations. (c) Misfit between observed and calculated age-depth observations, χ_s , as function of potential temperature and plate thickness, sliced at best fitting zero-age depth of 2.55 km; black cross = misfit minimum; red bar = optimal parameters when potential temperature is fixed at $1340 \pm 60^{\circ}\text{C}$. (d) Same for misfit between observed and calculated heat flow, χ_h . (e) Same for joint misfit, χ_t , between observed and calculated age-depth and heat flow observations, sliced at best fitting zero-age depth of 2.50 km; red cross = global minimum used to generate red curves in panels (a) and (b).

$\pm 13^{\circ}\text{C}$ change in predicted temperature but negligible change in either plate thickness or zero-age ridge depth. Varying thermal expansivity between its upper and lower bounds makes little difference to temperature and resulted in only a ± 2.5 km change in plate thickness, while zero-age ridge depth varied by ± 0.22 km. Finally, we adjust the temperature-dependence of thermal conductivity, in accordance with the upper and lower bounds of experimental measurements carried out by Schatz and Simmons (1972) and exploited by McKenzie et al. (2005). This variation yields a $\pm 115^{\circ}\text{C}$ change in optimal temperature, a ± 5 km change in plate thickness, and a minimal (i.e., ± 0.01 km) change in zero-age ridge depth.

From these tests, it is clear that the temperature dependence of thermal conductivity has the most significant effect upon the values of plate cooling parameters for this model (McKenzie et al., 2005). Modern experiments based upon laser flash analysis yield better resolved measurements with smaller uncertainties compared with the older measurements of Schatz and Simmons (1972) that use a contact method (Figure 7a; Hofmeister, 2005; Pertermann & Hofmeister, 2006). These later experiments also indicate that the original measurements of Schatz and Simmons (1972) together with the radiative conductivity parameterization of Hofmeister (1999), which were exploited by McKenzie et al. (2005), tend to underestimate the thermal conductivity of olivine by 20–30%. If, instead, we use a conductivity parameterization consistent with these more recent developments, uncertainty in the recovered value of T is reduced (Figure S1). Plate thickness and zero-age ridge depth now have acceptable values of 120 and 2.57 km, respectively. However, an increase in the value of k for olivine now yields an optimal potential temperature of 1106°C , which is $\sim 175^{\circ}\text{C}$ beneath the lower bound

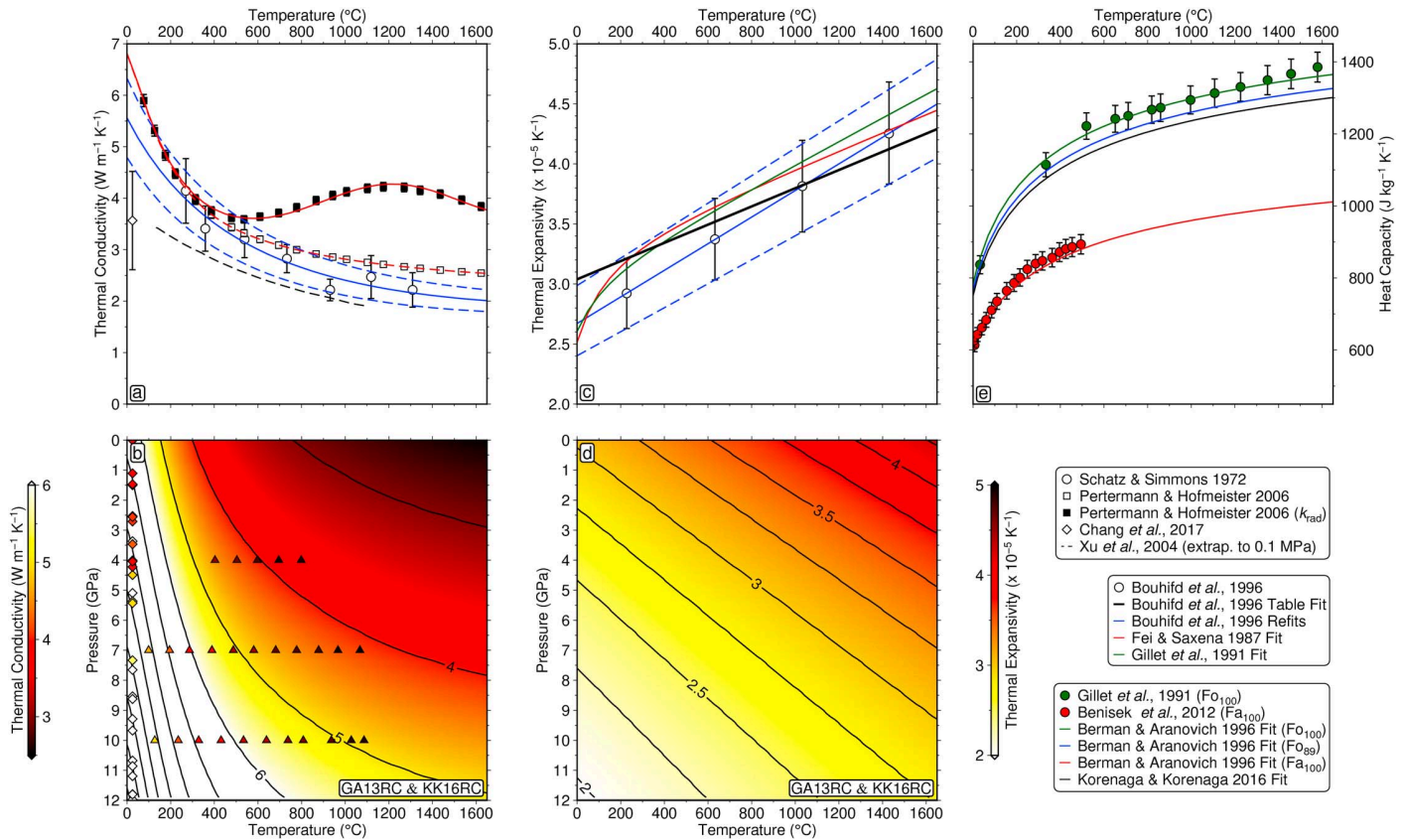


Figure 7. Temperature- and pressure-dependence of thermal conductivity, thermal expansivity and heat capacity. (a) Thermal conductivity plotted as function of temperature for constant pressure of 0.1 MPa. Squares with error bars and solid red line = forsterite lattice conductivity measurements from Pertermann and Hofmeister (2006) combined with 5 mm radiative conductivity measurements of Hofmeister (2005); triangles and red dashed line = forsterite lattice conductivity measurements from Pertermann and Hofmeister (2006); circles with error bars fitted with solid/dashed blue lines = forsterite conductivity measurements from Schatz and Simmons (1972) where dashed lines represent $\pm 1\sigma$; diamond with error bar = forsterite lattice conductivity measurement for anhydrous olivine from Chang et al. (2017); dashed black line = forsterite lattice conductivity at 0.1 MPa from equation (12) of Xu et al. (2004). (b) Contour map of forsterite lattice thermal conductivity as function of temperature and pressure based upon fitting measurements from Pertermann and Hofmeister (2006) using pressure dependence of Hofmeister (2007). Diamonds = forsterite lattice conductivity measurements for anhydrous olivine data from Chang et al. (2017); inverted triangles = forsterite lattice conductivity measurements from Xu et al. (2004). (c) Thermal expansivity of forsterite plotted as function of temperature for constant pressure of 0.1 MPa. Circles with error bars refitted with solid/dashed blue lines = measurements from Bouhifd et al. (1996) where dashed lines represent $\pm 1\sigma$; black line = relationship given in Table 2 of Bouhifd et al. (1996); red/green lines = relationships used by Fei and Saxena (1987) and Gillet et al. (1991), respectively. (d) Contour map of thermal expansivity of forsterite as function of temperature and pressure based upon parameterization of Grose and Afonso (2013) and Korenaga and Korenaga (2016). (e) Heat capacity plotted as function of temperature. Circles with error bars and red line = fayalite measurements from Benisek et al. (2012) fitted using fayalite parameterization of Berman (1988); triangles with error bars and green line = forsterite measurements from Gillet et al. (1991) using forsterite parameterization of Berman (1988); blue line = parameterization of Berman (1988) assuming 11% fayalite and 89% forsterite; black line = parameterization described by equation (2) of Korenaga and Korenaga (2016). Note that pressure dependence of heat capacity over the relevant range of plate thicknesses is negligible (Hofmeister, 2007).

of independent constraints. Optimal thermal parameters for subsidence and heat flow data still do not coincide. We therefore infer that the physics of lithospheric cooling is not adequately represented by an olivine-based, purely temperature-dependent model alone.

Experimental observations demonstrate that thermal conductivity and expansivity (but not specific heat capacity) vary significantly over pressure ranges relevant to lithospheric plates (Figures 7b and 7d; Hofmeister, 2007). We have incorporated the pressure dependency of k and α into a revised plate model (Table 1). Once again, an adequate fit to subsidence and heat flow observations is obtained where the residual value of χ_t is less than 1 (Figure S2). In this case, the global minimum shifts slightly to $T = 1102^{\circ}\text{C}$, $z_p = 140 \text{ km}$ and $z_r = 2.64 \text{ km}$. We conclude that the inclusion of pressure dependence alone makes little discernible difference to the potential temperature discrepancy.

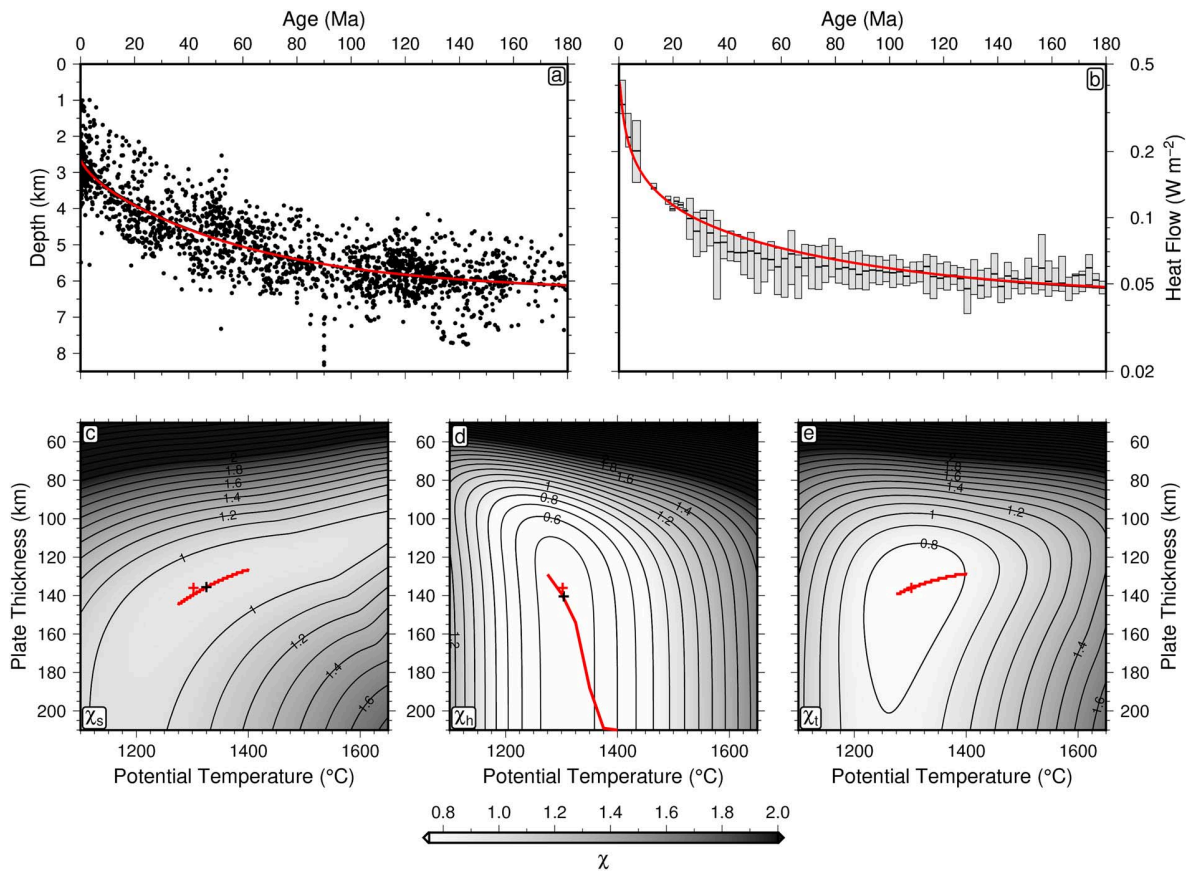


Figure 8. Complete plate model with 7-km-thick crustal layer. (a) Water-loaded depth to oceanic basement as function of plate age (Figure 2d); black line = optimal relationship obtained by only fitting age-depth observations; red line = optimal relationship from joint fit of age-depth and heat flow observations. (b) Surface heat flow as function of plate age (Figure 3c); gray boxes with horizontal bars = interquartile ranges of sediment-corrected heat flow measurements and median values; black line = optimal relationship obtained by only fitting heat flow observations; red line = optimal relationship from joint fit of age-depth and heat flow observations. (c) Misfit between observed and calculated age-depth observations, χ_s , as function of potential temperature and plate thickness, sliced at best fitting zero-age depth of 2.60 km; black cross = misfit minimum; red bar = optimal parameters when potential temperature is fixed at $1340 \pm 60^\circ\text{C}$. (d) Same for misfit between observed and calculated heat flow, χ_h . (e) Same for joint misfit, χ_t , between observed and calculated age-depth and heat flow observations, sliced at best fitting zero-age depth of 2.65 km; red cross = global minimum used to generate red curves in panels (a) and (b). Note that subsidence and heat flow misfit minima give similar values of potential temperature and plate thickness.

5.2.2. Complete Plate Models

Finally, we explore one additional issue that may help to resolve the temperature discrepancy. Although the assumption of pure olivine may be used as a reasonable approximation for the thermal properties of oceanic mantle lithosphere, this mineral constitutes $< 5\%$ of oceanic crust (White & Klein, 2013). Instead, plagioclase feldspar is the dominant phase ($\sim 50\%$) and the remainder is mostly pyroxene. Plagioclase has a thermal conductivity which is $\sim 25\%$ that of olivine. Thus the oceanic crustal layer tends to have an insulating effect with respect to the underlying mantle lithosphere. Grose and Afonso (2013) use a geometric mixing rule to estimate the conductivity of an aggregate consisting of plagioclase feldspar, diopside and olivine. This synthetic aggregate yields a conductivity of $2.65 \text{ W m}^{-1} \text{ K}^{-1}$ at room temperature and pressure. Ocean drilling program results report thermal conductivities of $\sim 2 \text{ W m}^{-1} \text{ K}^{-1}$ for basalt and gabbro at equivalent conditions (Kelemen et al., 2004). These values are smaller than the geometric mean calculated by Grose and Afonso (2013) but they are more consistent with the results of a harmonic mean mixing rule which yields $2.21 \text{ W m}^{-1} \text{ K}^{-1}$.

A revised plate model that incorporates a 7-km-thick low conductivity crustal layer yields $T = 1302^\circ\text{C}$, $z_p = 136 \text{ km}$, and $z_r = 2.64 \text{ km}$ (Figure 8). This result holds irrespective of whether a constant value of $k = 2 \text{ W m}^{-1} \text{ K}^{-1}$ is assumed, or whether a temperature-dependent conductivity based upon a harmonic mean of the parameterization described by Grose and Afonso (2013) is used (Table 1). Fixing the potential temperature at 1333°C yields only a 3% increase in residual misfit to the combined subsidence and heat flow databases

(Figures 8a and 8b). More significantly, we obtain consistent values of T , z_p and z_r , regardless of whether subsidence and heat flow measurements are jointly, or separately, fitted (Figures 8c, 8d and 8e). The recovered potential temperature of 1302°C lies within the range of independent constraints (i.e., $1340 \pm 60^\circ\text{C}$). The 2.6 ± 0.3 km zero-age depth is within the 2.85 ± 0.5 km bounds determined from global analyses of mid-ocean ridge depths (Dalton et al., 2014; Gale et al., 2014).

6. Implications

6.1. Intraplate Earthquakes

Thermal models of oceanic lithosphere are used to track individual isothermal contours as a function of plate age (Figure 9). It is instructive to compare alternative thermal models with depths of intraplate earthquakes in order to place constraints on the rheologic behavior of oceanic lithosphere. Wiens and Stein (1983) showed that the maximum depth of oceanic intraplate seismicity is bounded by the 700 – 800°C isothermal contour taken from the plate model of Parsons and Sclater (1977). They concluded that, above this temperature, oceanic lithosphere cannot support the stresses required to achieve brittle failure on seismogenic timescales. McKenzie et al. (2005) revisited this topic and argued that most intraplate earthquakes occur at depths that are cooler than the 600°C isothermal surface. Subsequently, Craig et al. (2014) reanalyzed the source parameters of earthquakes that occur in the vicinity of outer rises of oceanic plates. By combining their results with the thermal model of McKenzie et al. (2005), they suggested that the seismic-aseismic transition matched the 600°C isothermal surface, in good agreement with other seismological and experimental studies that determined an upper limit of 600°C .

In contrast, our revised thermal model suggests that the seismic-aseismic transition better matches the 700°C isothermal surface (Figure 9c). This revised estimate is a consequence of jointly fitting revised databases of both subsidence and heat flow observations, as well as incorporating the effects of pressure-dependence and a low conductivity crust. Our joint-fitting strategy yields an equilibrium plate thickness of 136 km, which is 30 km thicker than that proposed by McKenzie et al. (2005). The 100°C difference between our results and those of Craig et al. (2014) is significant and has obvious implications for plate rheology. Boettcher et al. (2007) provide a compelling argument which suggests that the strength and frictional behavior of olivine aggregates is consistent with a transition from velocity weakening to velocity strengthening at approximately 600°C . Following Goetze (1978), who carried out indentation creep tests on single olivine crystals, they calculate the yield stress at an asperity, σ_a , from

$$\sigma_a = \sigma_p \left(1 - \sqrt{\frac{-RT}{H} \ln \frac{\dot{\epsilon}}{B}} \right) \quad (19)$$

where the Peierl's stress $\sigma_p = 8500$ MPa, the molar gas constant $R = 8.314$ J mol $^{-1}$ K $^{-1}$, the activation enthalpy $H = 540$ kJ mol $^{-1}$, and the reference strain rate $B = 5.7 \times 10^{11}$ s $^{-1}$. The original form of this equation is given by Stocker and Ashby (1973) and by Goetze (1978). It arises from the fact that at low temperatures, the glide motion of dislocations within the crystal lattice become dominant. In nonmetals such as olivine, the lattice itself resists dislocation motion so that a finite, and often large, stress is required to move a dislocation. Thus, the Peierl's stress represents frictional resistance. Attempts to formulate rate equations for plastic flow in the rate limiting case are not wholly satisfactory but the observations are reasonably well described by equation (19). Dislocation flow in this high stress regime is sometimes referred to as the power law breakdown regime. Goetze (1978) compiled low pressure creep experiments that were carried out on dry polycrystalline olivine aggregates, which he used to determine the linear relationship between σ_a and \sqrt{T} . In Figure 10a, we have refitted these measurements so that the vertical intercept yields $\sigma_p = 8900 \pm 400$ MPa and the slope yields $H = 513$ kJ mol $^{-1}$.

One of the largest uncertainties in applying these experiments to geologic examples arises from the necessary extrapolation from laboratory strain rates of $\sim 10^{-5}$ s $^{-1}$ to rates of $\sim 10^{-13}$ s $^{-1}$. An equally important factor is uncertainty in the value of H , the activation enthalpy. Goetze (1978) summarizes experimental data which suggest that $H = 523 \pm 63$ kJ mol $^{-1}$. Subsequently, a considerable number of studies have refined this value to $H = 535 \pm 35$ kJ mol $^{-1}$ (e.g., Kirby & Kronenberg, 1987; Kohlstedt & Goetze, 1974; Kohlstedt et al., 1995). Following Boettcher et al. (2007), we extrapolate the results of Goetze (1978) to geologic strain rates of 10^{-15} – 10^{-12} s $^{-1}$ (Figure 10b). However, we conclude that this extrapolation suggests that the switch from a velocity weakening to velocity strengthening regime, regarded as a proxy for the seismic-aseismic transition, may occur at a higher temperature of $700 \pm 50^\circ\text{C}$, rather than 600°C as Boettcher et al. (2007) state.

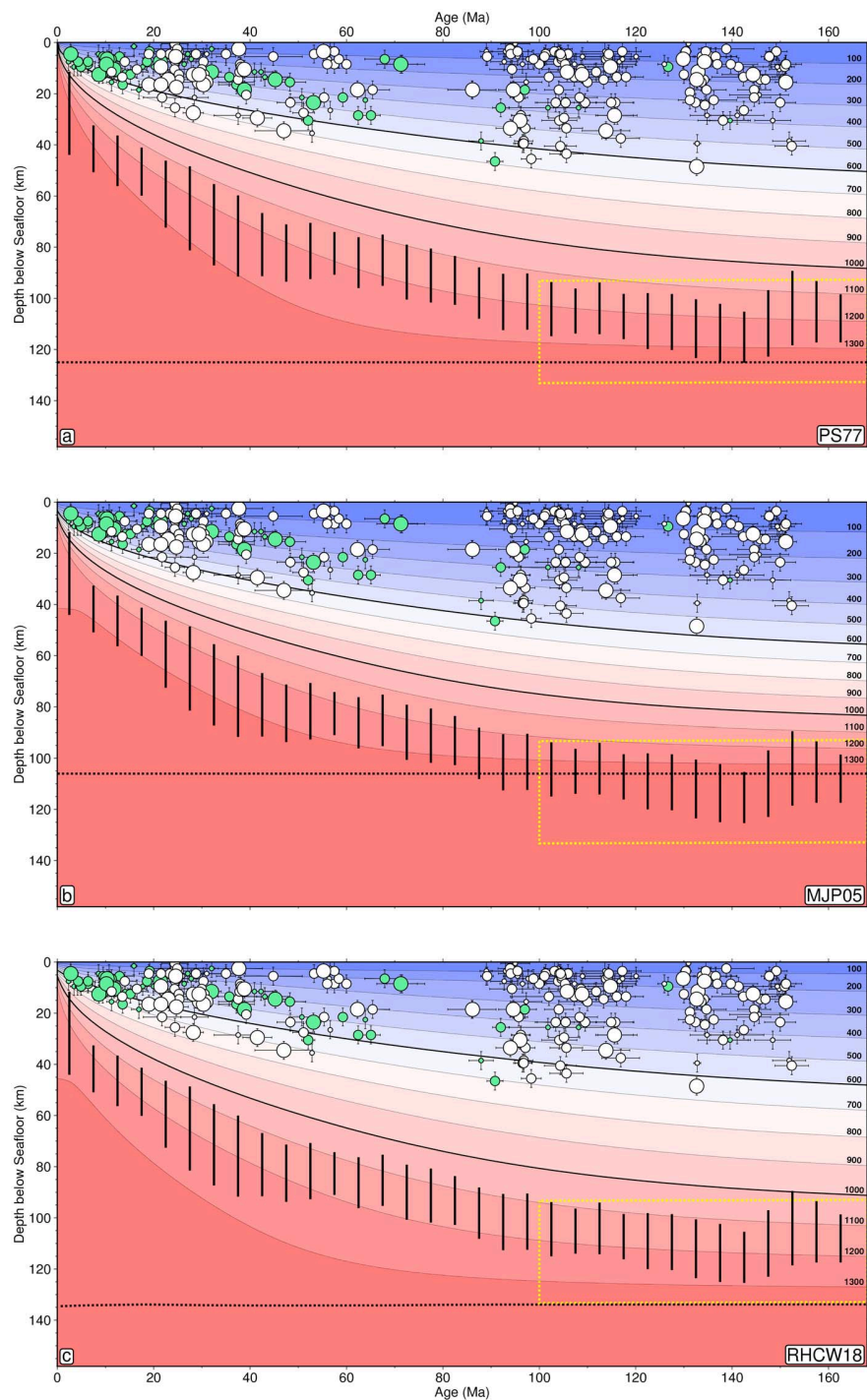


Figure 9. Thermal structure of oceanic lithosphere. (a) Simple analytical plate model using the published values reported by Parsons and Sclater (1977); numbered contours = isothermal surfaces plotted in $^{\circ}\text{C}$; green and white circles with error bars = oceanic intraplate and outer rise earthquakes from Craig et al. (2014) where small/medium/large circles = $M_b < 5.5$, $5.5 - 6.5$, and > 6.5 ; vertical black bars = depth to lithosphere-asthenosphere boundary in the Pacific Ocean based upon peak variations in azimuthal anisotropy (Burgos et al., 2014); dashed box = envelope of depths to lithosphere-asthenosphere boundary for plate ages > 100 Ma (Steinberger & Becker, 2016); horizontal black dashed line = base of plate model. (b) Same for the purely temperature-dependent plate model using parameter values from McKenzie et al. (2005). (c) Same for our optimal complete plate model using updated P-T-dependence of thermal parameters and a 7 km layer of oceanic crust.

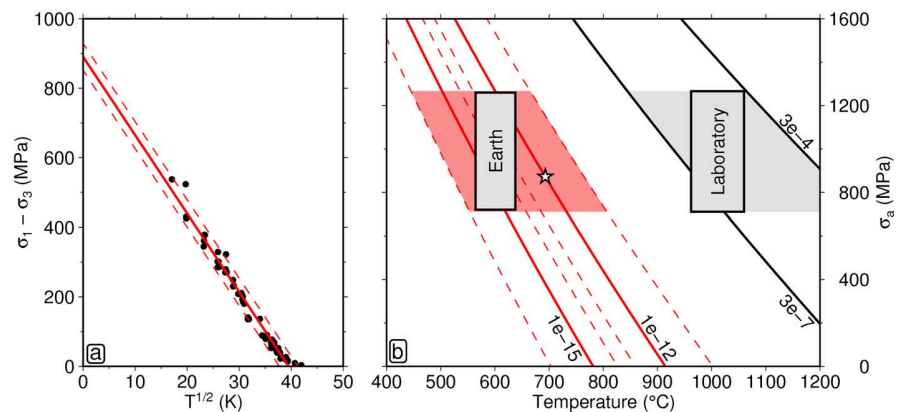


Figure 10. Rheologic scaling calculations. (a) Asperity stress, σ_a , plotted as function of temperature, \sqrt{T} , for suite of experimental measurements carried out on dry polycrystalline olivine aggregates, redigitised from Goetze (1978). Solid circles = creep measurements corrected to reference strain rate of 10^{-5} s^{-1} ; solid/dashed red lines = best-fitting linear relationship $\pm 2\sigma$ uncertainty. (b) Scaling between laboratory experiments and geologic conditions redrawn from Boettcher et al. (2007). Labeled black lines = relationships between σ_a and T for observed (laboratory) strain rates; labeled red lines = relationships between σ_a and T for extrapolated (geologic) strain rates (pairs of red dashed lines show variations arising from uncertainty in the activation enthalpy $H = 540 \pm 40 \text{ kJ mol}^{-1}$; labeled gray boxes = conditions at which transition from velocity-weakening to velocity-strengthening behavior occurs taken from Boettcher et al. (2007); gray/red polygons = temperature estimates for σ_a range of 800–1200 MPa; star = temperature estimate from optimal complete plate model for base of seismogenic zone (Figure 9c).

This revised temperature estimate is consistent with our thermal model (Figure 9c and Table S1) and with more recent laboratory studies (King & Marone, 2012).

6.2. Lithospheric Thickness Measurements

A range of seismologic approaches have been used to estimate lithospheric thickness across the oceanic realm. Unfortunately, this topic is complicated by a plethora of seismologic definitions for this boundary. They include the depth to a particular velocity contour, the depth at which lateral velocity variations cease, the depth of maximum negative velocity gradient, the depth to which conductive cooling extends, the depth at which there is a marked change in anisotropy, and the depth at which attenuation peaks (e.g., Eaton et al., 2009). Body and surface wave tomographic studies suggest that lateral velocity variations as a function of age persist down to depths of $\sim 150 \text{ km}$ (Priestley & McKenzie, 2013). Steinberger and Becker (2016) determine the evolution of lithospheric thickness by defining a critical isotherm, $T_L = T_0 + \phi(T - T_0)$, where $T_0 = 0^{\circ}\text{C}$ is surface temperature, T represents the geochemically constrained mantle potential temperature of 1333°C , and $\phi = 0.843$ is an arbitrary fraction of the temperature difference corresponding to the lithosphere-asthenosphere boundary. By applying this relationship to different tomographic models, Steinberger and Becker (2016) estimate an average depth to the lithosphere-asthenosphere boundary beneath old oceanic lithosphere of $109 \pm 22 \text{ km}$. These studies provide useful bounds but suffer from poor vertical resolution so that predicted lithosphere-asthenosphere boundaries determined by tomographic inverse modeling are rather dependent upon the starting model.

ScS reverberations, SS precursors, Sp, and Ps conversions can be generated by impedance contrasts at depth and they can also be used to place constraints on lithospheric thickness (Rychert et al., 2012; Schmerr, 2012). While these estimates have improved vertical resolution, independent information about velocity structure above the putative discontinuity is required to spatially position events by depth migration. It is also unclear whether or not the imaged discontinuities represent the actual lithosphere-asthenosphere boundary. A plausible alternative suggestion is that these discontinuities represent frozen-in radial anisotropy related to decompression melting at the ridge axis (Auer et al., 2015; Hansen et al., 2016). They could also be generated by trapped metasomatic melts that are frozen against the wet solidus (Pilet et al., 2011).

Deep seismic reflection and wide-angle experiments have been carried out in an attempt to image the transition from the high-velocity lithospheric lid to a lower velocity zone (e.g., Stern et al., 2015; Thybo, 2006). These tentative results are broadly consistent with the depth of peak azimuthal anisotropy variations and of shear wave gradients determined by Burgos et al. (2014), who obtained thicknesses of $\sim 115 \text{ km}$ for older ocean

basins (Figure 9). Bagley and Revenaugh (2008) and Kawakatsu et al. (2009) obtained values of 90–120 km for lithosphere that is > 100 Ma from the Pacific plate. It is important to emphasize that the depth to the lithosphere-asthenosphere boundary is not necessarily expected to coincide with a given isothermal surface since rheologic transitions are undoubtedly dependent upon confining pressure and strain rate (Hansen et al., 2016). Nonetheless, many studies adopt a temperature of 1100°C for the critical isothermal surface with the realistic range being $1120 \pm 80^\circ\text{C}$ (Pollack & Chapman, 1977; Steinberger & Becker, 2016).

Isothermal surfaces calculated using half-space cooling models strongly crosscut the seismologically determined lithospheric thicknesses at old ages. This discrepancy further suggests that such models are a poor representation of oceanic thermal structure. As lithosphere cools and thickens over time, the temperature of the rheological transition—if it changes at all—would be expected to increase rather than decrease as a consequence of increasing confining pressure. The best-fitting simple (i.e., constant parameter) plate model and the temperature-dependent model that implements the parameterization of McKenzie et al. (2005) both tend to underpredict lithospheric thickness (Table S1). However, a complete (i.e., compressible temperature- and pressure-dependent) model yields a satisfactory match with seismologically constrained estimates of the lithosphere-asthenosphere boundary. Notably, the peak change in orientation of azimuthal anisotropy observed in the Pacific Ocean appears to be strongly related to the $1175 \pm 50^\circ\text{C}$ isotherm (Burgos et al., 2014; Figure 9c). This match strengthens the validity of our optimal thermal structure.

An area of considerable ongoing debate is the relationship between elastic thickness and thermal structure of oceanic lithosphere. Some studies suggest that there is no consistent link between plate age and elastic thickness (e.g., Bry & White, 2007; Craig & Copley, 2014). Others have found an increase with age compatible with a cooling and mechanically strengthening plate (Hunter & Watts, 2016; Watts & Zhong, 2000). For the elastic thickness measurements compiled by Watts et al. (2013), 98% are bounded by the 700°C isotherm of the plate model obtained in this study.

6.3. Residual Depth Analysis

Cooling and thickening of oceanic lithosphere plays a dominant role in controlling both bathymetry and heat flow. Significant departures from this overall behavior yield insights into other geologic processes. For example, there is interest in isolating residual depth anomalies throughout the oceanic realm since these anomalies can be regarded as a bound on dynamic topography generated by mantle convective processes. Hoggard et al. (2016) show that the spectral properties of these residual depth anomalies do not strongly depend upon the precise reference model. Even so, it is instructive to check the extent to which residual depth measurements are influenced by alternative thermal models. Residual depth anomalies calculated using the half-space cooling model are significantly offset away from zero with substantial variance (Figure 11a). Anomalies calculated using our optimal plate model are symmetric about zero irrespective of plate age with negligible skewness and a standard deviation of ± 0.65 km (Figure 11c). In this case, the pattern, amplitude and wavelength of residual depth anomalies is similar to those determined by Hoggard et al. (2017).

Several residual depth studies argue that, if a half-space cooling model is used as a reference model, a large amount of dynamic support is predicted for older plate ages. It is important to emphasize that this model fails to adequately characterize the average thermal structure of oceanic lithosphere and that it is unable to fit well-known independent geophysical and geochemical constraints. Although the mechanism that supplies extra heat to the base of the plate to generate flattening of subsidence after ~ 60 Ma is often debated, it is a general feature of old oceanic lithosphere (Korenaga, 2015).

It has been suggested that residual depth anomalies could represent “frozen-in” thermal anomalies generated at the ridge axis itself (Marty & Cazenave, 1989). To test this hypothesis, we have run thermal models for plate thicknesses of 80–150 km using a range of axial temperature anomalies that are compatible with the geochemically inferred range (i.e., 1315 – 1550°C ; Dalton et al., 2014). The initial basal temperature is fixed through time, and the resulting subsidence patterns are compared. This modeling suggests that mean and maximum differences in predicted subsidence are 280–430 and 300–530 m, respectively. An average amplitude of ± 175 m for these severe tests suggests that putative ridge-generated thermal anomalies are unlikely to be the prime cause of residual depth anomalies. The lack of symmetric distributions of residual depths on either side of ridge axes, together with sequence stratigraphic geometries that corroborate the existence of residual depth anomalies adjacent to continental margins, are consistent with a subplate origin (e.g., Czarnota et al., 2013; Hoggard et al., 2017).

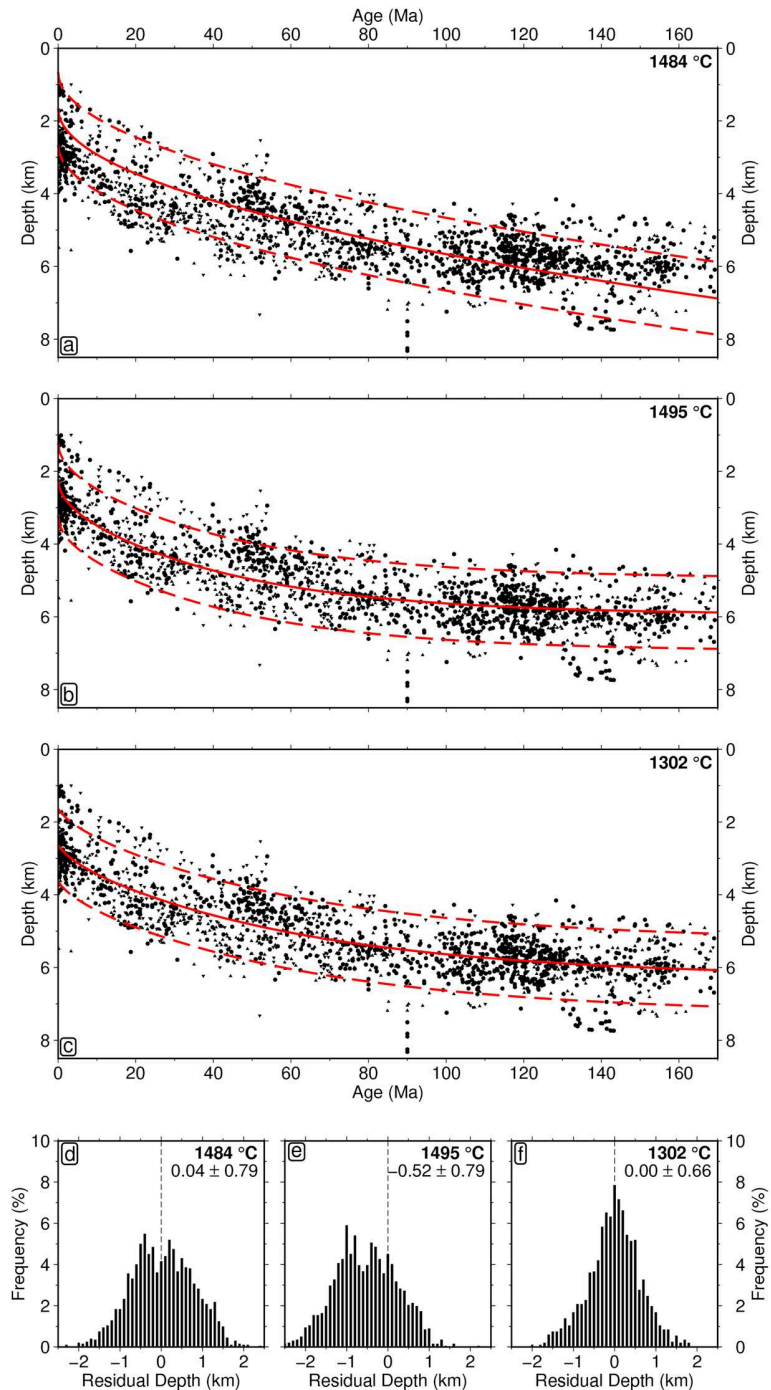


Figure 11. Residual depth anomalies. (a) Water-loaded depth to oceanic basement observations plotted as function of plate age (Figure 2d); solid/dashed red lines = optimal age-depth relationship ± 1 km from half-space cooling obtained for joint fit of subsidence and heat flow observations, which has axial temperature of 1484°C. (b) Same for simple analytical plate model, which has basal temperature of 1495°C. (c) Same for complete plate model, which has potential temperature of 1302°C. (d) Histogram of residual depth anomalies with respect to half-space cooling model shown in panel (a). Mean and standard deviation in top right-hand corner. (e) Same with respect to simple plate model shown in panel (b). (f) Same with respect to complete plate model shown in panel (c).

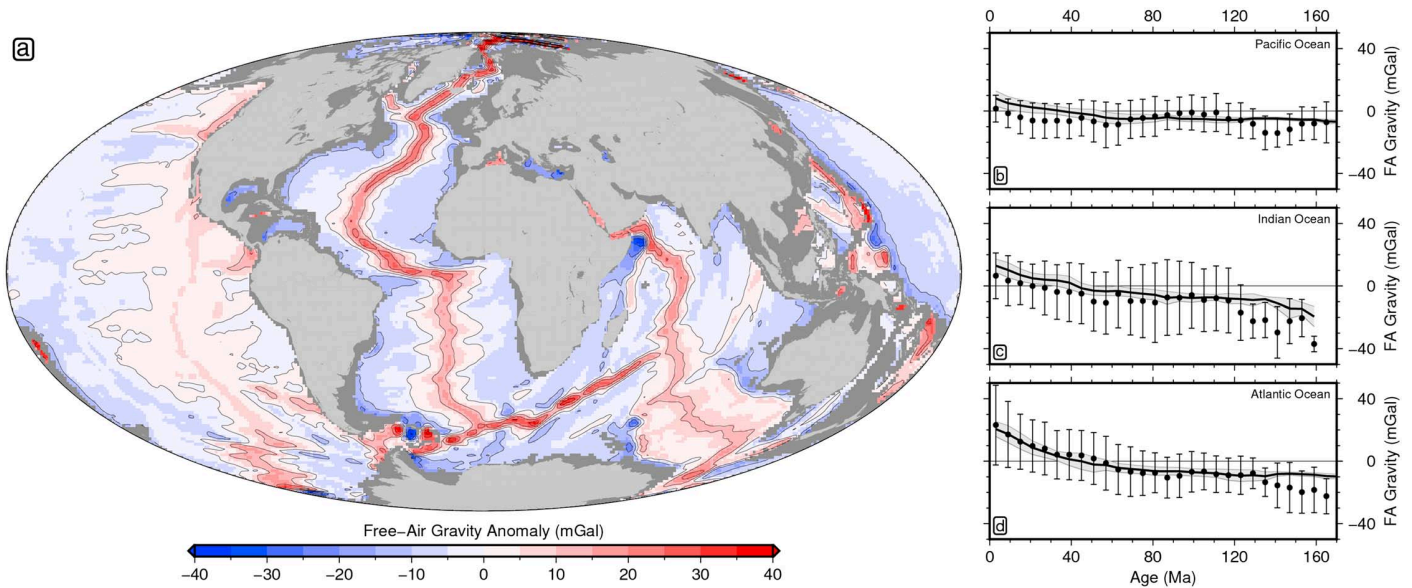


Figure 12. Observed and calculated free-air gravity anomalies. (a) Gravity field predicted from optimal complete plate model and updated age grid; contour interval = 10 mGal. (b) Solid line/gray envelope = mean and standard deviation of predicted gravity anomalies for Pacific Ocean binned as function of plate age; solid circles with vertical bars = observed stacked gravity field (Sandwell et al., 2014). (c) Same for Indian Ocean. (d) Same for Atlantic Ocean.

6.4. Gravitational Response of Plate Model

Our optimal thermal model can be used to calculate gravity anomalies generated by plate spreading, from which residual features related to flexure and mantle convection can be isolated in observed gravity fields. Here we follow the approach outlined by Crosby et al. (2006). First, our adapted oceanic age grid is expanded in terms of spherical harmonic coefficients, up to and including degree 90. Second, a grid of anomalous gravitational potential values, $\Delta U(x, y)$, is calculated from this filtered age grid using

$$\Delta U(x, y) = -2\pi G \left[\frac{(\rho_m - \rho_w)w(x, y)^2}{2} + \int_0^{z_p} z \Delta \rho(x, y, z) dz \right], \quad (20)$$

where $\Delta \rho$ is the density contrast between a vertical column of hot asthenosphere at the ridge axis and a column of cooling lithosphere away from the ridge axis, w is plate subsidence, z_p is plate thickness, $z = 0$ is at the seabed, ρ_m is mantle density at 0°C and ρ_w is the density of water. Thirdly, the grid of $\Delta U(x, y)$ values is fitted using real spherical harmonics up to degree 120, generating a suite of coefficients C_{lm} and S_{lm} where l and m represent degree and order, respectively. The predicted free-air gravity field can then be calculated using

$$\Delta g = -\frac{1}{R} \sum_{l=0}^{120} (l+1) \sum_{m=0}^l [C_{lm} \cos(m\lambda) + S_{lm} \sin(m\lambda)] \bar{P}_{lm}(\cos \theta), \quad (21)$$

where \bar{P}_{lm} is the normalized Legendre polynomial, λ is longitude, θ is co-latitude and $R = 6371$ km is the Earth's radius (Figure 12a).

Isolating a corresponding plate cooling signal from satellite-based gravity observations is complicated by superposition of other unrelated signals within the waveband of interest. While this complication rules out the use of gravitational predictions as a direct constraint on thermal evolution, we note that the chosen plate model matches large-scale features. In particular, the general reduction of spreading rates from the Pacific, through Indian and into the Atlantic oceans generates an increasingly large anomaly on young oceanic lithosphere that is matched by observed gravity anomalies (Figures 12b–12d). The negative gravity anomaly observed in the Pacific Ocean at ages < 70 Ma correlates with a long-wavelength gravity signal, implying that negative dynamic topography near the East Pacific Rise ridge axis may be responsible for deviations away from a plate cooling signal in this part of the basin (Figure 12b).

7. Discussion

Previous attempts to constrain the thermal evolution of oceanic lithosphere using temperature and pressure-dependent parameters have either independently fixed temperature at the ridge axis or inves-

tigated a narrow range of potential temperatures (Grose & Afonso, 2013; Korenaga & Korenaga, 2016; McKenzie et al., 2005). Here we simultaneously vary ridge depth, potential temperature, and plate thickness for an appropriate range of values in order to identify global minima. This approach enables inconsistencies between parameter values required to fit either subsidence or heat flow observations to be identified and investigated. It is important that model complexity is only increased in order to decrease misfit and to improve parameter determination.

An important aim is to constrain the globally-averaged behavior of oceanic lithosphere. Other studies of oceanic plate evolution have investigated regional differences in subsidence and heat flow measurements (Crosby et al., 2006; Parsons & Sclater, 1977). In order to investigate any regional variation in optimal parameters, we have repeated our analysis using subsidence and heat flow databases from individual oceanic basins. It is clear that parameters can vary between different basins. For example, the Pacific Ocean yields a thin, cool plate and intermediate zero-age ridge depths (i.e., $T = 1223^{\circ}\text{C}$, $z_p = 123$ km, $z_r = 2.75$ km; Figure S3). The Indian Ocean requires a similarly thin plate with hotter underlying temperatures and deeper zero-age ridge depths (i.e., $T = 1270^{\circ}\text{C}$, $z_p = 120$ km, $z_r = 2.91$ km; Figure S4). In contrast, the Atlantic Ocean has a thick plate with intermediate temperatures and shallow ridge depths (i.e., $T = 1253^{\circ}\text{C}$, $z_p = 177$ km, $z_r = 2.34$ km; Figure S5). These regional variations probably reflect the local interplay between dynamic topography and background plate cooling, highlighting the primary importance of using global databases to sidestep spatial bias. In the Atlantic Ocean, for example, known hot spots tend to coincide with younger lithosphere (e.g., Iceland, Azores, Ascension, St. Helena, and Tristan da Cunha), but such spatial bias is less evident in the Pacific Ocean. Notwithstanding these caveats, optimal global parameters yield basin-by-basin misfit values that are only 9%, 7%, and 5% greater than individual minima for the Pacific, Atlantic, and Indian Oceans, respectively. Thus, given available data constraints, there is no compelling argument for systematic differences in plate cooling behavior between basins.

As thermal models become more physically realistic, discrepancies between the optimal parameters required to individually fit subsidence and heat flow observations have reduced, together with overall misfit (Tables 1, S2, and S3). This tendency would appear to validate application of temperature- and pressure-dependent parameterizations for thermal properties based upon laboratory experiments and their scalability. It has been suggested in previous studies that experimentally determined thermal expansivity values may lead to overestimates of thermal contraction for the Earth, giving rise to underestimates of potential temperature (Grose, 2012; Korenaga, 2007a; Pollack, 1980). However, we note that our optimal model has $T = 1302^{\circ}\text{C}$, which is broadly consistent with the geochemically quoted range of $T = 1340 \pm 60^{\circ}\text{C}$. We can obtain a value of $T = 1340^{\circ}\text{C}$ if thermal expansivity is arbitrarily reduced by $\sim 1\%$, which is well within the $\pm 0.3 \times 10^{-5} \text{ K}^{-1}$ experimental uncertainty bounds (Bouhifd et al., 1996). Consequently, it may not be necessary to appeal to incomplete thermal relaxation or to differences in mineral assemblage in order to account for the apparent expansivity deficit (cf. Grose & Afonso, 2013; Korenaga, 2007b).

The effects of phase changes are difficult to assess since experimental constraints on thermal expansivity, heat capacity and conductivity at the relevant P - T conditions are not available for many mineral constituents (Schutt & Leshner, 2006). Conditions at phase changes and the associated density transformations are also dependent upon composition, volatile content, and oxidation state, all of which remain uncertain (Jennings & Holland, 2015). As a result, we think that implementation of age-dependent phase changes is not required at present since it introduces additional degrees of freedom. Korenaga and Korenaga (2016) use the pMELTS algorithm to determine the effects of melt extraction and phase changes on equilibrium mineral assemblages, but much of the thermodynamic database they exploit relies upon parameter estimations or upon extrapolation of temperature and pressure derivatives that sometimes depart from experimental constraints (Berman, 1988; Ghiorso et al., 2002; Ueki & Iwamori, 2013). Although their approximation of the temperature and pressure dependence for C_p and k_{rad} yield improved results compared with those of Grose and Afonso (2013), their inferred increase in subsidence rate of $\sim 80 \text{ m Ma}^{-1}$ at $\sim 20 \text{ Ma}$, attributed to the spinel-garnet transition, cannot currently be identified within age-depth observations (Figure 2d).

A significant difference between the temperature- and pressure-dependent plate model proposed here and previous models is that the equilibrated plate thickness is slightly greater and neither expansivity nor conductivity have been artificially adjusted. A thicker plate reflects both a smaller thermal contraction at the base of the plate as a result of the increase in confining pressure and the insulating effect of low conductivity oceanic crust, which reduces the rate of heat extraction. This latter effect gives rise to slightly lower poten-

tial temperatures compared with strictly temperature-dependent models that do not include a crustal layer (e.g., McKenzie et al., 2005). The thicker plate retrieved using a compressible model is consistent with seismologic constraints (Burgos et al., 2014; Goutorbe, 2010; Steinberger & Becker, 2016; Figure 9).

Thermal models can also be used to investigate the Earth's heat budget. The estimated total surface heat flow is 46 ± 3 TW, of which 29.7 ± 1.3 TW conducts out of the oceanic plates, as estimated from previous cooling models (Davies & Davies, 2010; Hasterok, 2013; Jaupart & Mareschal, 2007; Lay & Buffett, 2008; Pollack et al., 1993). This value can be revised by combining our oceanic age grid with

$$Q = \int_0^{t_{\max}} H(t) \frac{dA}{dt} dt \quad (22)$$

where A is total seafloor area of a given age, t_{\max} is maximum seafloor age, and $H(t)$ is the predicted surface heat flow for that age.

The revised plate model yields a total oceanic heat flow of $Q = 27.5$ TW, which increases to $Q = 28.0$ TW if mantle potential temperature is fixed at 1333°C (Table 1). These values are $\sim 7\%$ lower than previous estimates. For comparison, a plate model without temperature or pressure dependence and low-conductivity crust yields $Q \sim 32.7$ TW. Total heat flow therefore decreases by ~ 5 TW when P-T-dependence and a lower conductivity crustal layer are included, giving rise to a similar overall heat flux but at reduced potential temperatures. We note that the integrated conductive heat flow into the base of the oceanic plate is 4.7 TW for the revised thermal model, suggesting that $\sim 17\%$ of surface heat flow is provided by resupply of heat beneath older oceanic plates away from the ridge axis.

8. Conclusions

A range of different thermal models have been used to fit a combined database of oceanic basement depths and corrected heat flow measurements. In this way, we have attempted to isolate an optimal temperature structure of oceanic lithosphere. Models are compared with seismologic and petrologic constraints on plate thickness, melt generation, and rheologic structure. A half-space cooling model yields less satisfactory fits to combined observations for plate ages > 100 Ma, in comparison with plate cooling models. As temperature dependence, pressure dependence and a low-conductivity crustal layer are progressively incorporated into the plate model, residual misfit reduces, and potential temperature and plate thickness estimates converge upon independently determined values, validating recent mineral physics results. A significant contribution to the difference between our revised model and previous models is the insulating effect of the low-conductivity oceanic crust.

Our revised plate model has a zero-age depth of 2.6 ± 0.3 km, a potential temperature of $1300 \pm 60^\circ\text{C}$ and a plate thickness of 135 ± 30 km. The recovered potential temperature is compatible with that required to generate 7 km of oceanic crust from an anhydrous lherzolite source and it is broadly consistent with geochemical constraints determined from mid-oceanic ridge basalts. This model provides a reasonable fit to variations in the gravitational field and also yields residual depth anomalies that are evenly distributed with minimal skewness. Integrated surface heat flow through oceanic lithosphere is estimated at ~ 28 TW, which is slightly lower than previous estimates. The base of the seismogenic zone tracks the 700°C isothermal surface and a temperature of $1175 \pm 50^\circ\text{C}$ agrees with lithosphere-asthenosphere boundary estimates derived from the depth to peak variations in azimuthal anisotropy as a function of plate age.

References

- Afonso, J. C., Ranalli, G., & Fernández, M. (2007). Density structure and buoyancy of the oceanic lithosphere revisited. *Geophysical Research Letters*, 34, L10302. <https://doi.org/10.1029/2007GL029515>
- Auer, L., Becker, T. W., Boschi, L., & Schmerr, N. (2015). Thermal structure, radial anisotropy, and dynamics of oceanic boundary layers. *Geophysical Research Letters*, 42, 9740–9749. <https://doi.org/10.1002/2015GL066246>
- Bagley, B., & Revenaugh, J. (2008). Upper mantle seismic shear discontinuities of the Pacific. *Journal of Geophysical Research*, 113, 301. <https://doi.org/10.1029/2008JB005692>
- Benisek, A., Kroll, H., & Dachs, E. (2012). The heat capacity of fayalite at high temperatures. *American Mineralogist*, 97, 657–660.
- Berman, R. G. (1988). Internally-consistent thermodynamic data for minerals in the system $\text{Na}_2\text{O}-\text{K}_2\text{O}-\text{CaO}-\text{MgO}-\text{FeO}-\text{Fe}_2\text{O}_3-\text{Al}_2\text{O}_3-\text{SiO}_2-\text{TiO}_2-\text{H}_2\text{O}-\text{CO}_2$. *Journal of Petroleum*, 29(2), 445–522. <https://doi.org/10.1093/petrology/29.2.445>
- Berman, R. G., & Aranovich, L. Y. (1996). Optimized standard state and solution properties of minerals 1. Model calibration for olivine, orthopyroxene, cordierite, garnet, ilmenite in the system $\text{FeO}-\text{MgO}-\text{CaO}-\text{Al}_2\text{O}_3-\text{TiO}_2-\text{SiO}_2$. *Contributions to Mineralogy and Petrology*, 126(1-2), 1–24. <https://doi.org/10.1007/s004100050233>

Acknowledgments

This research is supported by BP Exploration. F. D. R. acknowledges support from Natural Environment Research Council and the Schmidt Science Fellows program, in partnership with the Rhodes Trust. M. J. H. acknowledges support from the National Aeronautics and Space Administration grant NNX17AE17G. We are grateful to Spectrum Geo and to ION Geophysical for permission to publish reflection profiles shown in Figures 2b and 2c, respectively. We thank J. C. Afonso, P. Bellingham, A. Bump, T. Craig, A. Crosby, I. Frame, S. Ghelichkhan, S. Goes, C. Grose, L. Hansen, N. Hodgson, B. Horn, S. Humbert, M. Ireland, D. Lyness, K. McDermott, D. McKenzie, C. Richardson, O. Shorttle, S. Stephenson, and J. Winterbourne for their help. Figures were prepared using Generic Mapping Tools software. Observations and models are provided in the supporting information and in an online repository of the University of Cambridge (<https://doi.org/10.17863/CAM.26215>). The authors declare no competing financial interests. University of Cambridge Earth Sciences contribution esc.4313.

- Boettcher, M. S., Hirth, G., & Evans, B. (2007). Olivine friction at the base of oceanic seismogenic zones. *Journal of Geophysical Research*, 112, B01205. <https://doi.org/10.1029/2006JB004301>
- Bouhifd, M. A., Andrault, D., Fiquet, G., & Richet, P. (1996). Thermal expansion of forsterite up to the melting point. *Geophysical Research Letters*, 23(10), 1143–1146. <https://doi.org/10.1029/96GL01118>
- Brown, E., & Leshner, C. (2016). REEBOX PRO: A forward model simulating melting of thermally and lithologically variable upwelling mantle. *Geochemistry, Geophysics, Geosystems*, 17, 3929–3968. <https://doi.org/10.1002/2016GC006579>
- Bry, M., & White, N. (2007). Reappraising elastic thickness variation at oceanic trenches. *Journal of Geophysical Research*, 112, B08414. <https://doi.org/10.1029/2005JB004190>
- Burgos, G., Montagner, J. P., Beucler, E., Capdeville, Y., Mocquet, A., & Drilleau, M. (2014). Oceanic lithosphere-asthenosphere boundary from surface wave dispersion data. *Journal of Geophysical Research: Solid Earth*, 119, 1079–1093. <https://doi.org/10.1002/2013JB010528>
- Chang, Y. Y., Hsieh, W. P., Tan, E., & Chen, J. (2017). Hydration-reduced lattice thermal conductivity of olivine in Earth's upper mantle. *Proceedings of the National Academy of Sciences*, 114(16), 4078–4081. <https://doi.org/10.1073/pnas.1616216114>
- Coffin, M. F., & Eldholm, O. (1994). Large igneous provinces: Crustal structure, dimensions, and external consequences. *Reviews of Geophysics*, 32(1), 1–36. <https://doi.org/10.1029/93RG02508>
- Craig, T. J., & Copley, A. (2014). An explanation for the age independence of oceanic elastic thickness estimates from flexural profiles at subduction zones, and implications for continental rheology. *Earth and Planetary Science Letters*, 392, 207–216.
- Craig, T. J., Copley, A., & Jackson, J. (2014). A reassessment of outer-rise seismicity and its implications for the mechanics of oceanic lithosphere. *Geophysical Journal International*, 197(1), 63–89. <https://doi.org/10.1093/gji/ggu013>
- Crosby, A. G., McKenzie, D., & Sclater, J. G. (2006). The relationship between depth, age and gravity in the oceans. *Geophysical Journal International*, 166(2), 553–573. <https://doi.org/10.1111/j.1365-246X.2006.03015.x>
- Czarnota, K., Hoggard, M. J., White, N., & Winterbourne, J. (2013). Spatial and temporal patterns of Cenozoic dynamic topography around Australia. *Geochemistry, Geophysics, Geosystems*, 14, 634–658. <https://doi.org/10.1029/2012GC004392>
- Dalton, C. A., Langmuir, C. H., & Gale, A. (2014). Geophysical and geochemical evidence for deep temperature variations beneath mid-ocean Ridges. *Science*, 344(6179), 80–83. <https://doi.org/10.1126/science.1249466>
- Davaille, A., & Jaupart, C. (1994). Onset of thermal convection in fluids with temperature-dependent viscosity: Application to the oceanic mantle. *Journal of Geophysical Research*, 99(B10), 19,853–19,866. <https://doi.org/10.1029/94JB01405>
- Davies, J. H., & Davies, D. R. (2010). Earth's surface heat flux. *Solid Earth*, 1(1), 5–24. <https://doi.org/10.5194/se-1-5-2010>
- Doin, M. P., & Fleitout, L. (1996). Thermal evolution of the oceanic lithosphere: An alternative view. *Earth and Planetary Science Letters*, 142, 121–136. [https://doi.org/10.1016/0012-821X\(96\)00082-9](https://doi.org/10.1016/0012-821X(96)00082-9)
- Eaton, D. W., Darbyshire, F., Evans, R. L., Grütter, H., Jones, A. G., & Yuan, X. (2009). The elusive lithosphere-asthenosphere boundary (LAB) beneath cratons. *Lithos*, 109(1–2), 1–22. <https://doi.org/10.1016/j.lithos.2008.05.009>
- Fei, Y., & Saxena, S. (1987). An equation for the heat capacity of solids. *Geochimica et Cosmochimica Acta*, 51, 251–254.
- Gale, A., Langmuir, C. H., & Dalton, C. A. (2014). The global systematics of ocean ridge basalts and their origin. *Journal of Petrology*, 55(6), 1051–1082. <https://doi.org/10.1093/ptrology/egu017>
- Galloway, W. E., Whiteaker, T. L., & Ganey-Curry, P. (2011). History of Cenozoic North American drainage basin evolution, sediment yield, and accumulation in the Gulf of Mexico basin. *Geosphere*, 7(4), 938–973. <https://doi.org/10.1130/GES00647.1>
- Ghiorso, M. S., Hirschmann, M. M., Reiners, P. W., & Kress, V. C. (2002). The pMELTS: A revision of MELTS for improved calculation of phase relations and major element partitioning related to partial melting of the mantle to 3 GPa. *Geochemistry, Geophysics, Geosystems*, 3(5), 1030. <https://doi.org/10.1029/2001GC000217>
- Gillet, P., Richet, P., Guyot, F., & Fiquet, G. (1991). High-temperature thermodynamic properties of forsterite. *Journal of Geophysical Research*, 96(B7), 11,805–11,816.
- Goetze, C. (1978). The mechanisms of creep in olivine. *Philosophical Transactions of the Royal Society A*, 288(1350), 99–119. <https://doi.org/10.1098/rsta.1978.0008>
- Goutorbe, B. (2010). Combining seismically derived temperature with heat flow and bathymetry to constrain the thermal structure of oceanic lithosphere. *Earth and Planetary Science Letters*, 295(3–4), 390–400. <https://doi.org/10.1016/j.epsl.2010.04.013>
- Grose, C. J. (2012). Properties of oceanic lithosphere: Revised plate cooling model predictions. *Earth and Planetary Science Letters*, 333–334, 250–264. <https://doi.org/10.1016/j.epsl.2012.03.037>
- Grose, C. J., & Afonso, J. C. (2013). Comprehensive plate models for the thermal evolution of oceanic lithosphere. *Geochemistry, Geophysics, Geosystems*, 14, 3751–3778. <https://doi.org/10.1002/ggge.20232>
- Guliyev, I. S., Mamedov, P. Z., Feyzullayev, A. A., Huseynov, D. A., Kadirov, F. A., Aliyeva, E. H. M., et al. (2003). *Hydrocarbon Systems of the South Caspian Basin*, (pp. 206). Baku: Nafta-Press.
- Hansen, L. N., Qi, C., & Warren, J. M. (2016). Olivine anisotropy suggests Gutenberg discontinuity is not the base of the lithosphere. *Proceedings of the National Academy of Sciences*, 113(38), 10,503–10,506. <https://doi.org/10.1073/pnas.1608269113>
- Hasterok, D. (2013). A heat flow based cooling model for tectonic plates. *Earth and Planetary Science Letters*, 361, 34–43. <https://doi.org/10.1016/j.epsl.2012.10.036>
- Hasterok, D., Chapman, D. S., & Davis, E. E. (2011). Oceanic heat flow: Implications for global heat loss. *Earth and Planetary Science Letters*, 311(3–4), 386–395. <https://doi.org/10.1016/j.epsl.2011.09.044>
- Herzberg, C., Asimow, P. D., Arndt, N., Niu, Y., Leshner, C. M., Fitton, J. G., et al. (2007). Temperatures in ambient mantle and plumes: Constraints from basalts, picrites, and komatiites. *Geochemistry, Geophysics, Geosystems*, 8, Q02006. <https://doi.org/10.1029/2006GC001390>
- Hillier, J. K., & Watts, A. B. (2005). Relationship between depth and age in the North Pacific Ocean. *Journal of Geophysical Research*, 110, B02405. <https://doi.org/10.1029/2004JB003406>
- Hofmeister, A. M. (1999). Mantle values of thermal conductivity and the geotherm from phonon lifetimes. *Science*, 283, 1699–1706. <https://doi.org/10.1126/science.283.5408.1699>
- Hofmeister, A. M. (2005). Dependence of diffusive radiative transfer on grain-size, temperature, and Fe-content: Implications for mantle processes. *Journal of Geodynamics*, 40, 51–72. <https://doi.org/10.1016/j.jog.2005.06.001>
- Hofmeister, A. M. (2007). Pressure dependence of thermal transport properties. *Proceedings of the National Academy of Sciences*, 104(22), 9192–9197.
- Hofmeister, A. M., & Pertermann, M. (2008). Thermal diffusivity of clinopyroxenes at elevated temperature. *European Journal of Mineralogy*, 20, 537–549.
- Hoggard, M. J., White, N., & Al-Attar, D. (2016). Global dynamic topography observations reveal limited influence of large-scale mantle flow. *Nature Geoscience*, 9, 456–463. <https://doi.org/10.1038/ngeo2709>
- Hoggard, M. J., Winterbourne, J., Czarnota, K., & White, N. (2017). Oceanic residual depth measurements, the plate cooling model and global dynamic topography. *Journal of Geophysical Research: Solid Earth*, 122, 2328–2372. <https://doi.org/10.1002/2016JB013457>

- Huang, J., & Zhong, S. (2005). Sublithospheric small-scale convection and its implications for the residual topography at old ocean basins and the plate model. *Journal of Geophysical Research*, 110, B05404. <https://doi.org/10.1029/2004JB003153>
- Hunter, J., & Watts, A. (2016). Gravity anomalies, flexure and mantle rheology seaward of circum-pacific trenches. *Geophysical Journal International*, 207(1), 288–316.
- Jaupart, C., & Mareschal, J. C. (2007). Heat flow and thermal structure of the lithosphere, *Treatise on Geophysics* (pp. 217–252). Amsterdam: Elsevier. <https://doi.org/10.1016/B978-0-444-53802-4.00114-7>
- Jennings, E. S., & Holland, T. J. B. (2015). A simple thermodynamic model for melting of peridotite in the system NCFMASOcr. *Journal of Petroleum*, 56(5), 869–892. <https://doi.org/10.1093/petrology/egv020>
- Katsura, T., Yamada, H., Nishikawa, O., Song, M., Kubo, A., Shinmei, T., et al. (2004). Olivine-wadsleyite transition in the system (Mg, Fe)₂SiO₄. *Journal of Geophysical Research*, 109, B02209. <https://doi.org/10.1029/2003JB002438>
- Katz, R. F., Spiegelman, M., & Langmuir, C. H. (2003). A new parameterization of hydrous mantle melting. *Geochemistry, Geophysics, Geosystems*, 4(9), 1073. <https://doi.org/10.1029/2002GC000433>
- Kawakatsu, H., Kumar, P., Takei, Y., Shinohara, M., Kanazawa, T., Araki, E., et al. (2009). Seismic evidence for sharp lithosphere-asthenosphere boundaries of oceanic plates. *Science*, 324(5926), 499–502.
- Kelemen, P., Kikawa, E., & Miller, D. (2004). Shipboard Scientific Party, Leg 209 Summary. In *Proc. ODP, Init. Repts.*, 209 (pp. 1–139). College Station, TX: Ocean Drilling Program.
- King, D. S. H., & Marone, C. (2012). Frictional properties of olivine at high temperature with applications to the strength and dynamics of the oceanic lithosphere. *Journal of Geophysical Research*, 117, B12203. <https://doi.org/10.1029/2012JB009511>
- Kirby, S. H., & Kronenberg, A. K. (1987). Rheology of the lithosphere: Selected topics. *Reviews of Geophysics*, 25(6), 1219–1244. <https://doi.org/10.1029/RG025i006p01219>
- Kohlstedt, D. L., Evans, B., & Mackwell, S. J. (1995). Strength of the lithosphere: Constraints imposed by laboratory experiments. *Journal of Geophysical Research*, 100(B9), 17,587–17,602. <https://doi.org/10.1029/95JB01460>
- Kohlstedt, D. L., & Goetze, C. (1974). Low-stress high-temperature creep in olivine single crystals. *Journal of Geophysical Research*, 79(14), 2045–2051. <https://doi.org/10.1029/JB079i014p02045>
- Korenaga, J. (2007a). Effective thermal expansivity of Maxwellian oceanic lithosphere. *Earth and Planetary Science Letters*, 257(1–2), 343–349. <https://doi.org/10.1016/j.epsl.2007.03.010>
- Korenaga, J. (2007b). Thermal cracking and the deep hydration of oceanic lithosphere: A key to the generation of plate tectonics? *Journal of Geophysical Research*, 112, B05408. <https://doi.org/10.1029/2006JB004502>
- Korenaga, J. (2015). Seafloor topography and the thermal budget of Earth. *Geological Society of America Specifications of Paper*, 514(11), 167–185. [https://doi.org/10.1130/2015.2514\(11\)](https://doi.org/10.1130/2015.2514(11))
- Korenaga, T., & Korenaga, J. (2008). Subsidence of normal oceanic lithosphere, apparent thermal expansivity, and seafloor flattening. *Earth and Planetary Science Letters*, 268(1), 41–51. <https://doi.org/10.1016/j.epsl.2007.12.022>
- Korenaga, T., & Korenaga, J. (2016). Evolution of young oceanic lithosphere and the meaning of seafloor subsidence rate. *Journal of Geophysical Research: Solid Earth*, 121, 6315–6332. <https://doi.org/10.1002/2016JB013395>
- Laske, G., Masters, G., Ma, Z., & Pasyanos, M. (2013). Update on CRUST1.0 - A 1-degree global model of Earth's crust. In *EGU General Assembly Conference Abstracts*, 15, pp. EGU2013–2658.
- Lay, T., & Buffett, B. (2008). Core - mantle boundary heat flow. *Nature Geoscience*, 1, 13–15. <https://doi.org/10.1038/ngeo.2007.44>
- Lister, C. R. B. (1972). On the thermal balance of a mid-ocean ridge. *Geophysical Journal International*, 26(5), 515–535. <https://doi.org/10.1111/j.1365-246X.1972.tb05766.x>
- Marty, J. C., & Cazenave, A. (1989). Regional variations in subsidence rate of oceanic plates: A global analysis. *Earth and Planetary Science Letters*, 94(3–4), 301–315. [https://doi.org/10.1016/0012-821X\(89\)90148-9](https://doi.org/10.1016/0012-821X(89)90148-9)
- Matthews, S., Shorttle, O., & MacLennan, J. (2016). The temperature of the Icelandic mantle from olivine-spinel aluminum exchange thermometry. *Geochemistry, Geophysics, Geosystems*, 17, 4725–4752. <https://doi.org/10.1002/2016GC006497>
- McKenzie, D. P. (1967). Some remarks on heat flow and gravity anomalies. *Journal of Geophysical Research*, 72(24), 6261–6273. <https://doi.org/10.1029/JZ072i024p06261>
- McKenzie, D., Jackson, J., & Priestley, K. (2005). Thermal structure of oceanic and continental lithosphere. *Earth and Planetary Science Letters*, 233(3–4), 337–349. <https://doi.org/10.1016/j.epsl.2005.02.005>
- Müller, R. D., Sdrolias, M., Gaina, C., & Roest, W. R. (2008). Age, spreading rates, and spreading asymmetry of the world's ocean crust. *Geochemistry, Geophysics, Geosystems*, 9, Q04006. <https://doi.org/10.1029/2007GC001743>
- Müller, R. D., Seton, M., Zahirovic, S., Williams, S. E., Matthews, K. J., Wright, N. M., et al. (2016). Ocean basin evolution and global-scale reorganization events since Pangea breakup. *Annual Review of Earth and Planetary Sciences*, 44(1), 107–138. <https://doi.org/10.1146/annurev-earth-060115-012211>
- Parsons, B., & McKenzie, D. (1978). Mantle convection and the thermal structure of the plates. *Journal of Geophysical Research*, 83(B9), 4485–4496. <https://doi.org/10.1029/JB083iB09p04485>
- Parsons, B., & Sclater, J. G. (1977). An analysis of the variation of ocean floor bathymetry and heat flow with age. *Journal of Geophysical Research*, 82(5), 803–827. <https://doi.org/10.1029/JB082i005p0803>
- Pertermann, M., & Hofmeister, A. M. (2006). Thermal diffusivity of olivine-group minerals at high temperature. *American Mineralogist*, 91(2005), 1747–1760. <https://doi.org/10.2138/am.2006.2105>
- Pilet, S., Baker, M. B., Müntener, O., & Stolper, E. M. (2011). Monte carlo simulations of metasomatic enrichment in the lithosphere and implications for the source of alkaline basalts. *Journal of Petrology*, 52(7–8), 1415–1442.
- Pollack, H. N. (1980). On the use of the volumetric thermal expansion coefficient in models of ocean floor topography. *Tectonophysics*, 64(3–4), T45–T47. [https://doi.org/10.1016/0040-1951\(80\)90095-5](https://doi.org/10.1016/0040-1951(80)90095-5)
- Pollack, H. N., & Chapman, D. S. (1977). On the regional variation of heat flow, geotherms, and lithospheric thickness. *Tectonophysics*, 38(3–4), 279–296. [https://doi.org/10.1016/0040-1951\(77\)90215-3](https://doi.org/10.1016/0040-1951(77)90215-3)
- Pollack, H. N., Hurter, S. J., & Johnson, J. R. (1993). Heat flow from the Earth's interior: Analysis of the global data set. *Reviews of Geophysics*, 31(3), 267–280. <https://doi.org/10.1029/93RG01249>
- Press, W. H., Teukolsky, S. A., Vetterling, W. T., & Flannery, B. P. (1992). *Numerical Recipes in C: The Art of Scientific Computing* (2nd Ed.). New York, NY, USA: Cambridge University Press.
- Priestley, K., & McKenzie, D. (2013). The relationship between shear wave velocity, temperature, attenuation and viscosity in the shallow part of the mantle. *Earth and Planetary Science Letters*, 381, 78–91. <https://doi.org/10.1016/j.epsl.2013.08.022>
- Rychert, C. A., Schmerr, N., & Harmon, N. (2012). The Pacific lithosphere-asthenosphere boundary: Seismic imaging and anisotropic constraints from SS waveforms. *Geochemistry, Geophysics, Geosystems*, 13, Q0AK10. <https://doi.org/10.1029/2012GC004194>

- Sandwell, D. T., Muller, R. D., Smith, W. H. F., Garcia, E., & Francis, R. (2014). New global marine gravity model from CryoSat-2 and Jason-1 reveals buried tectonic structure. *Science*, 346(6205), 65–67. <https://doi.org/10.1126/science.1258213>
- Schatz, J. F., & Simmons, G. (1972). Thermal conductivity of Earth materials at High Temperatures. *Journal of Geophysical Research*, 77(35), 6966–6983.
- Schmeling, H., Marquart, G., & Nawa, V. (2017). The role of hydrothermal cooling of the oceanic lithosphere for ocean floor bathymetry and heat flow. *Journal of Geophysical Research: Solid Earth*, 122, 3934–3952. <https://doi.org/10.1002/2016JB013881>
- Schmerr, N. (2012). The Gutenberg discontinuity: Melt at the lithosphere-asthenosphere boundary. *Science*, 335(6075), 1480–1483.
- Schutt, D. L., & Leshner, C. E. (2006). Effects of melt depletion on the density and seismic velocity of garnet and spinel lherzolite. *Journal of Geophysical Research*, 111, B05401. <https://doi.org/10.1029/2003JB002950>
- Slater, J. G., Jaupart, C., & Galson, D. (1980). The heat flow through oceanic and continental crust and the heat loss of the Earth. *Reviews of Geophysics*, 18(1), 269–311. <https://doi.org/10.1029/RG018i001p00269>
- Shorttle, O., MacLennan, J., & Lambart, S. (2014). Quantifying lithological variability in the mantle. *Earth and Planetary Science Letters*, 395, 24–40. <https://doi.org/10.1016/j.epsl.2014.03.040>
- Simmons, M., Tari, G., & Okay, A. (2018). Petroleum geology of the Black Sea: introduction. *Geological Society, London, Special Publications*, 464, SP464–15.
- Stein, C. A., & Stein, S. (1992). A model for the global variation in oceanic depth and heat flow with lithospheric age. *Nature*, 356(6391), 133–135.
- Steinberger, B., & Becker, T. W. (2016). A comparison of lithospheric thickness models. *Tectonophysics*. <https://doi.org/10.1016/j.tecto.2016.08.001>
- Stern, T. A., Henrys, S. A., Okaya, D., Louie, J. N., Savage, M. K., Lamb, S., et al. (2015). A seismic reflection image for the base of a tectonic plate. *Nature*, 518(7537), 85–88. <https://doi.org/10.1038/nature14146>
- Stockert, R. L., & Ashby, M. F. (1973). On the rheology of the upper mantle. *Reviews of Geophysics*, 11(2), 391–426. <https://doi.org/10.1029/RG011i002p00391>
- Thybo, H. (2006). The heterogeneous upper mantle low velocity zone. *Tectonophysics*, 416(1), 53–79. <https://doi.org/10.1016/j.tecto.2005.11.021>
- Turcotte, D. L., & Oxburgh, E. R. (1967). Finite amplitude convective cells and continental drift. *Journal of Fluid Mechanics Research*, 28(1), 29–42. <https://doi.org/10.1017/S0022112067001880>
- Turcotte, D. L., & Oxburgh, E. R. (1969). Convection in a mantle with variable physical properties. *Journal of Geophysical Research*, 74(6), 1458–1474. <https://doi.org/10.1029/JB074i006p01458>
- Turcotte, D. L., & Schubert, G. (2002). *Geodynamics*, 2nd ed., (pp. 472). Cambridge: Cambridge University Press.
- Ueki, K., & Iwamori, H. (2013). Thermodynamic model for partial melting of peridotite by system energy minimization. *Geochemistry, Geophysics, Geosystems*, 14, 342–366. <https://doi.org/10.1029/2012GC004143>
- Von Herzen, R. P., & Uyeda, S. (1963). Heat flow through the eastern Pacific ocean floor. *Journal of Geophysical Research*, 68(14), 4219–4250. <https://doi.org/10.1029/JZ068i014p04219>
- Waples, D. W., & Waples, J. S. (2004). A review and evaluation of specific heat capacities of rocks, minerals, and subsurface fluids. Part 2: Fluids and porous rocks. *Natural Resources Research*, 13, 123–130. <https://doi.org/10.1023/B:NARR.0000032648.15016.49>
- Watts, A. B., & Zhong, S. (2000). Observations of flexure and the rheology of oceanic lithosphere. *Geophysical Journal International*, 142(3), 855–875. <https://doi.org/10.1046/j.1365-246X.2000.00189.x>
- Watts, A., Zhong, S., & Hunter, J. (2013). The behavior of the lithosphere on seismic to geologic timescales. *Annual Review of Earth and Planetary Sciences*, 41, 443–468. <https://doi.org/10.1146/annurev-earth-042711-105457>
- Wessel, P., Sandwell, D. T., & Kim, S.-S. (2010). The global seamount census. *Oceanography*, 23(1), 24–33.
- White, W. M., & Klein, E. M. (2013). Composition of the Oceanic Crust, *Treatise on Geochemistry* (pp. 457–496). Amsterdam: Elsevier. <https://doi.org/10.1016/B978-0-08-095975-7.00315-6>
- White, R. S., McKenzie, D., & O'Nions, R. K. (1992). Oceanic crustal thickness from seismic measurements and rare earth element inversions. *Journal of Geophysical Research*, 97(B13), 19,683–19,715. <https://doi.org/10.1029/92JB01749>
- Whittaker, J. M., Goncharov, A., Williams, S. E., Müller, R. D., & Leitchenkov, G. (2013). Global sediment thickness data set updated for the Australian-Antarctic Southern Ocean. *Geochemistry, Geophysics, Geosystems*, 14, 3297–305. <https://doi.org/10.1002/ggge.20181>
- Wiens, D. A., & Stein, S. (1983). Age dependence of oceanic intraplate seismicity and implications for lithospheric evolution. *Journal of Geophysical Research*, 88(B8), 6455–6468. <https://doi.org/10.1029/JB088iB08p06455>
- Xu, Y., Shankland, T. J., Linhardt, S., Rubie, D. C., Langenhorst, F., & Klasinski, K. (2004). Thermal diffusivity and conductivity of olivine, wadsleyite and ringwoodite to 20 GPa and 1373 K. *Physics of the Earth and Planetary Interiors*, 143(1-2), 321–336. <https://doi.org/10.1016/j.pepi.2004.03.005>
- Yuen, D. A., & Fleitout, L. (1985). Thinning of the lithosphere by small-scale convective destabilization. *Nature*, 313(5998), 125–128.



Journal of Geophysical Research: Solid Earth

Supporting Information for

**Reassessing the Thermal Structure of Oceanic Lithosphere with Revised Global
Inventories of Basement Depths and Heat Flow Measurements**

Fred D. Richards^{1,2}, Mark J. Hoggard², Laurence R. Cowton³, and Nicky J. White¹

¹Department of Earth Sciences, Bullard Laboratories, Madingley Rise, Madingley Road, Cambridge, CB3 0EZ, UK

²Department of Earth & Planetary Sciences, Harvard University, 20 Oxford Street, Cambridge, MA 02138, USA

³ASI Data Science, 54 Welbeck Street, London, W1G 9XS, UK.

Corresponding Authors: Fred D. Richards (frichards@schmidtsciencefellows.org)

Mark J. Hoggard (mark_hoggard@fas.harvard.edu)

Nicky J. White (njw10@cam.ac.uk)

Contents

1. Details of density parameterizations used in temperature- and pressure-dependent plate models.
2. Figure showing results of temperature-dependent model using updated olivine conductivity parameterization (Figure S1).
3. Figure showing results of temperature- and pressure-dependent model using updated olivine conductivity parameterization (Figure S2).
4. Figures showing results of complete plate model with 7-km-thick crustal layer for individual ocean basins (Pacific, Indian and Atlantic; Figures S3-S5).
5. Figure showing results of complete half-space cooling model with 7-km-thick crustal layer (Figure S6).
6. Table comparing seismogenic thickness and lithosphere-asthenosphere boundary predictions of different models (Table S1).
7. Table comparing results of optimal model with previously proposed thermal models (Table S2).
8. Table comparing optimal parameters for different models when fitted to subsidence and heat flow constraints separately (Table S3).
9. Notation table (Table S4).

Additional Supporting Information (Files uploaded separately)

10. Adapted lithospheric age grid of *Müller et al.* (2016), augmented by including oceanic crust from the Black Sea, Caspian Sea, eastern Mediterranean Sea, New Caledonian and Aleutian basins, in GMT grid format (Figures 2a and 3a). Gridding artefacts within the Gulf of California and along the Mohns Ridge are also corrected using age constraints taken from *Müller et al.* (2008).
11. Water-loaded basement depth observations. Global dataset shown in Figures 2d, 4a, 5a, 6a, 8a, S1a, S2a and S6a; Pacific in Figure S3a; Indian in Figure S4a and Atlantic in Figure S5a. Data are in ASCII format.
12. Corrected heat flow observations. Global dataset shown in Figures 3a, 4b, 5b, 6b, 8b, S1b, S2b and S6b; Pacific in Figure S3b; Indian in Figure S4b and Atlantic in Figure S5b. Data are in ASCII format.
13. Basement depths predicted by optimal plate model in ASCII format (Figure 8a).
14. Heat flow predicted by optimal plate model in ASCII format (Figure 8b).
15. Thermal structure of optimal plate model in GMT grid format (Figure 9c).

See key in table below for file name explanations. Alternatively, all original files with clear names are available on the University of Cambridge online repository (<https://doi.org/10.17863/CAM.26215>). Please email me if you have any trouble.

Explanation of supplementary data file names.

File Name	File Contents
2018JB015998-sup-0002-Data Set SI-S01_AA.grd	Revised and augmented oceanic age grid
2018JB015998-sup-0003-Data Set SI-S02_AA.zip	Water-loaded basement depth observations (global, Pacific, Indian and Atlantic).
2018JB015998-sup-0004-Data Set SI-S03_AA.zip	Corrected heat flow observations (global, Pacific, Indian and Atlantic).
2018JB015998-sup-0005-Data Set SI-S04_AA.zip	Predicted basement depths of optimal and geochemically constrained complete plate models
2018JB015998-sup-0006-Data Set SI-S05_AA.zip	Predicted heat flow of optimal and geochemically constrained complete plate models
2018JB015998-sup-0007-Data Set SI-S06_AA.zip	Thermal structure of optimal and geochemically constrained complete plate models

Density Parameterizations

Temperature-Dependent Parameterizations

For temperature dependent parameterizations, following the approach of *McKenzie et al.* (2005), density is given by

$$\rho = \rho_0 \exp \left(-\alpha_0(T - T_0) - \frac{\alpha_1}{2}(T^2 - T_0^2) \right). \quad (1)$$

α_0 and α_1 are calibrated constants derived from mineral physics experiments that describe the temperature dependence of thermal expansivity, $\rho_0 = 3.33 \text{ Mg m}^{-3}$ and $T_0 = 273 \text{ K}$.

Temperature and Pressure-Dependent Parameterizations

For temperature and pressure-dependent parameterizations the approach of *Grose and Afonso* (2013) is adopted to determine density. First, isothermal volume change $(V_0/V)_T$ is calculated from pressure at each timestep using a Brent minimization algorithm and the third-order Birch-Murnaghan equation of state

$$P = \frac{3}{2}K_0 \left[\left(\frac{V_0}{V} \right)_T^{\frac{7}{3}} - \left(\frac{V_0}{V} \right)_T^{\frac{5}{3}} \right] \left\{ 1 + \frac{3}{4}(K'_T - 4) \left[\left(\frac{V_0}{V} \right)_T^{\frac{2}{3}} - 1 \right] \right\} \quad (2)$$

where $K_0 = 130 \text{ GPa}$ is the bulk modulus at $P = 0$ and $K'_T = 4.8$ is the pressure derivative of the isothermal bulk modulus. Having calculated isothermal volume change, isothermal density change as a function of pressure can then be calculated using

$$\rho(P) = \rho_0 \left(\frac{V_0}{V} \right)_T. \quad (3)$$

Next the pressure dependence of thermal expansivity as a function of temperature is determined using

$$\frac{\alpha(P, T)}{\alpha(T)} = \left(\frac{V_0}{V} \right)_T \exp \left\{ (\delta_T + 1) \left[\left(\frac{V_0}{V} \right)_T^{-1} - 1 \right] \right\} \quad (4)$$

where $\delta_T = 6$ is the Grüneisen parameter. This expression then allows for density to be calculated as a function of temperature and pressure using

$$\rho(P, T) = \rho(P) \left(1 - \frac{\alpha(P, T)}{\alpha(T)} \int_{T_0}^T \alpha(T) dT \right). \quad (5)$$

Since the pressure effect in oceanic crust is minor, the same expressions and moduli are applied to the crustal layer.

T-Dependent Model with Updated Olivine Conductivity

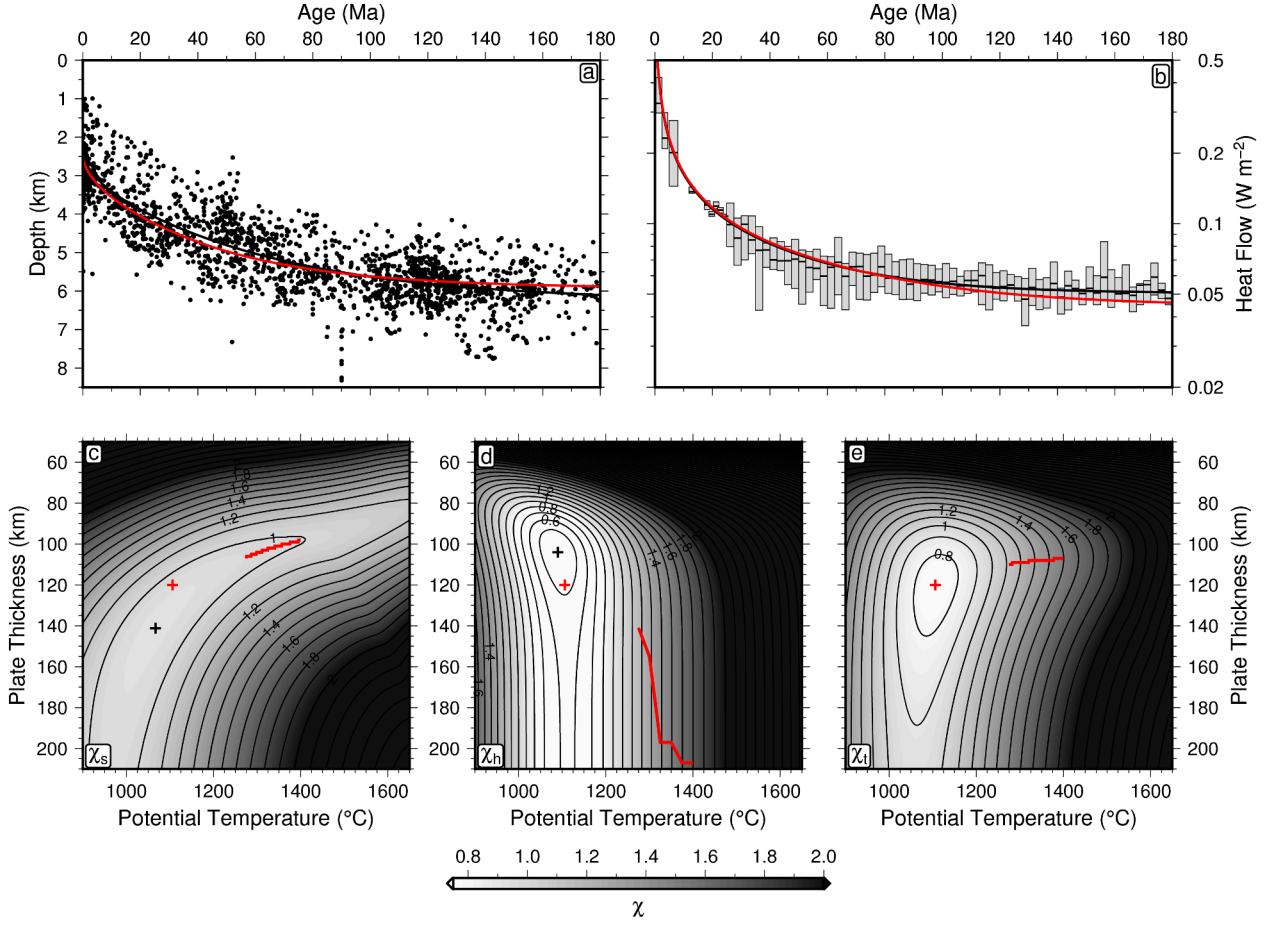


Figure S1: **Temperature-dependent plate model with updated conductivity parameterizations and no oceanic crust.** (a) Water-loaded depth to oceanic basement as function of plate age (Figure 2d); black line = optimal relationship obtained by only fitting age-depth observations; red line = optimal relationship from joint fit of age-depth and heat flow observations. (b) Surface heat flow as function of plate age (Figure 3c); gray boxes with horizontal bars = interquartile ranges of sediment-corrected heat flow measurements and median values; black line = optimal relationship obtained by only fitting heat flow observations; red line = optimal relationship from joint fit of age-depth and heat flow observations. (c) Misfit between observed and calculated age-depth observations, χ_s , as function of potential temperature and plate thickness, sliced at best fitting zero-age depth of 2.45 km; black cross = misfit minimum; red bar = optimal parameters when potential temperature is fixed at $1340 \pm 60^\circ\text{C}$. (d) Same for misfit between observed and calculated heat flow, χ_h . (e) Same for joint misfit, χ_t , between observed and calculated age-depth and heat flow observations, sliced at best fitting zero-age depth of 2.55 km; red cross = global minimum used to generate red curves in panels (a) and (b).

T- & *P*- Dependent Model with Updated Olivine Conductivity

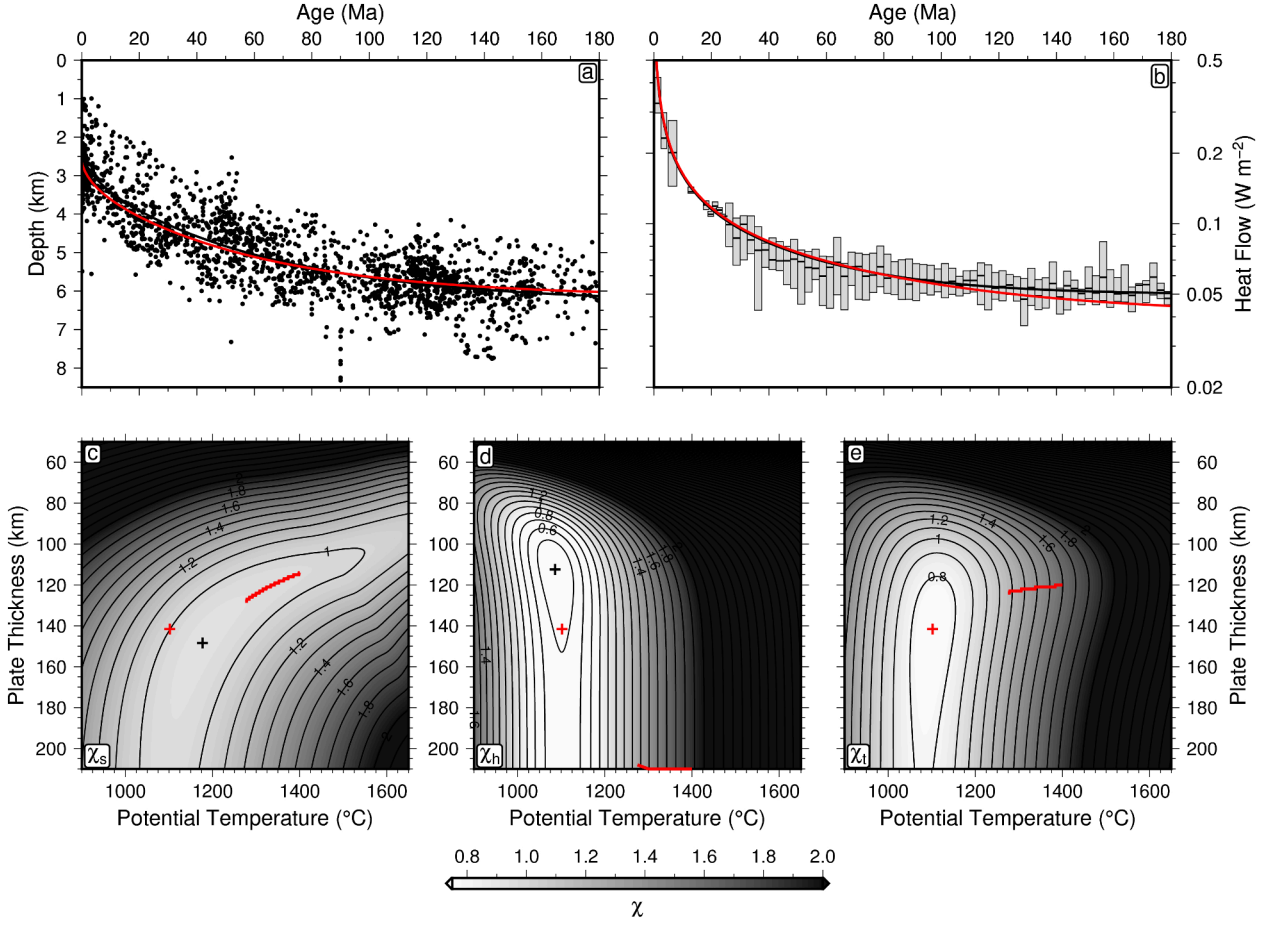


Figure S2: **Temperature- and pressure-dependent plate model with updated conductivity parameterizations and no oceanic crust.** (a) Water-loaded depth to oceanic basement as function of plate age (Figure 2d); black line = optimal relationship obtained by only fitting age-depth observations; red line = optimal relationship from joint fit of age-depth and heat flow observations. (b) Surface heat flow as function of plate age (Figure 3c); gray boxes with horizontal bars = interquartile ranges of sediment-corrected heat flow measurements and median values; black line = optimal relationship obtained by only fitting heat flow observations; red line = optimal relationship from joint fit of age-depth and heat flow observations. (c) Misfit between observed and calculated age-depth observations, χ_s , as function of potential temperature and plate thickness, sliced at best fitting zero-age depth of 2.45 km; black cross = misfit minimum; red bar = optimal parameters when potential temperature is fixed at $1340 \pm 60^\circ\text{C}$. (d) Same for misfit between observed and calculated heat flow, χ_h . (e) Same for joint misfit, χ_t , between observed and calculated age-depth and heat flow observations, sliced at best fitting zero-age depth of 2.65 km; red cross = global minimum used to generate red curves in panels (a) and (b).

Complete Plate Models for Individual Ocean Basins

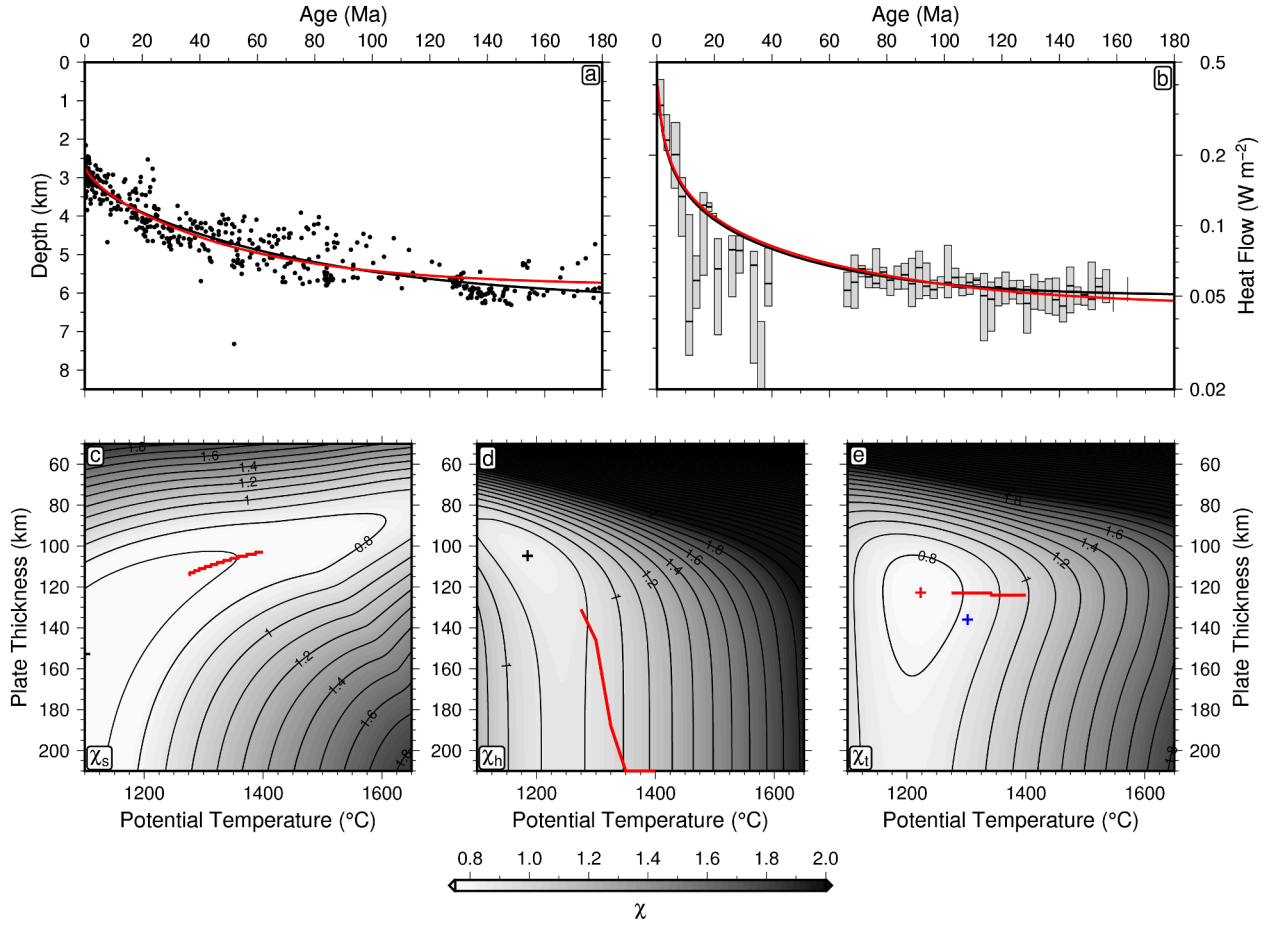


Figure S3: **Complete plate model with input data from Pacific Ocean only.** (a) Water-loaded depth to oceanic basement as function of plate age (Figure 2d); black line = optimal relationship obtained by only fitting age-depth observations; red line = optimal relationship from joint fit of age-depth and heat flow observations. (b) Surface heat flow as function of plate age (Figure 3c); gray boxes with horizontal bars = interquartile ranges of sediment-corrected heat flow measurements and median values; black line = optimal relationship obtained by only fitting heat flow observations; red line = optimal relationship from joint fit of age-depth and heat flow observations. (c) Misfit between observed and calculated age-depth observations, χ_s , as function of potential temperature and plate thickness, sliced at best fitting zero-age depth of 2.85 km; black cross = misfit minimum; red cross = joint misfit minimum used to generate red curves in panels (a) and (b); red bar = optimal parameters when potential temperature is fixed at $1340 \pm 60^\circ\text{C}$. (d) Same for misfit between observed and calculated heat flow, χ_h . (e) Same for joint misfit, χ_t , between observed and calculated age-depth and heat flow observations, sliced at best fitting zero-age depth of 2.75 km; red cross = global minimum used to generate red curves in panels (a) and (b); blue cross = global minimum of global dataset.

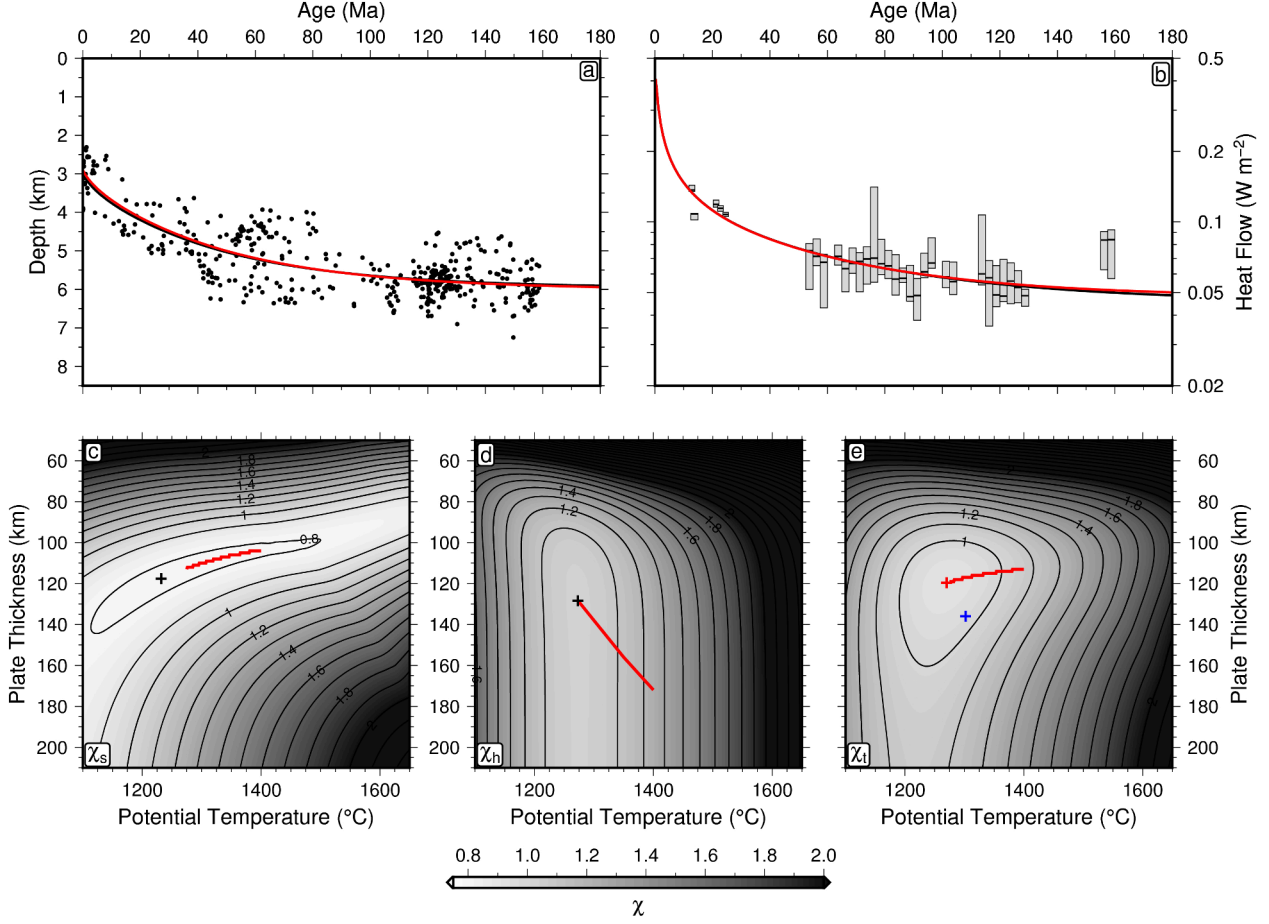


Figure S4: **Complete plate model with input data from Indian Ocean only.** (a) Water-loaded depth to oceanic basement as function of plate age (Figure 2d); black line = optimal relationship obtained by only fitting age-depth observations; red line = optimal relationship from joint fit of age-depth and heat flow observations. (b) Surface heat flow as function of plate age (Figure 3c); gray boxes with horizontal bars = interquartile ranges of sediment-corrected heat flow measurements and median values; black line = optimal relationship obtained by only fitting heat flow observations; red line = optimal relationship from joint fit of age-depth and heat flow observations. (c) Misfit between observed and calculated age-depth observations, χ_s , as function of potential temperature and plate thickness, sliced at best fitting zero-age depth of 3.00 km; black cross = misfit minimum; red cross = joint misfit minimum used to generate red curves in panels (a) and (b); red bar = optimal parameters when axial temperature is fixed at $1340 \pm 60^{\circ}\text{C}$. (d) Same for misfit between observed and calculated heat flow, χ_h . (e) Same for joint misfit, χ_t , between observed and calculated age-depth and heat flow observations, sliced at best fitting zero-age depth of 2.90 km; red cross = global minimum used to generate red curves in panels (a) and (b); blue cross = global minimum of global dataset.

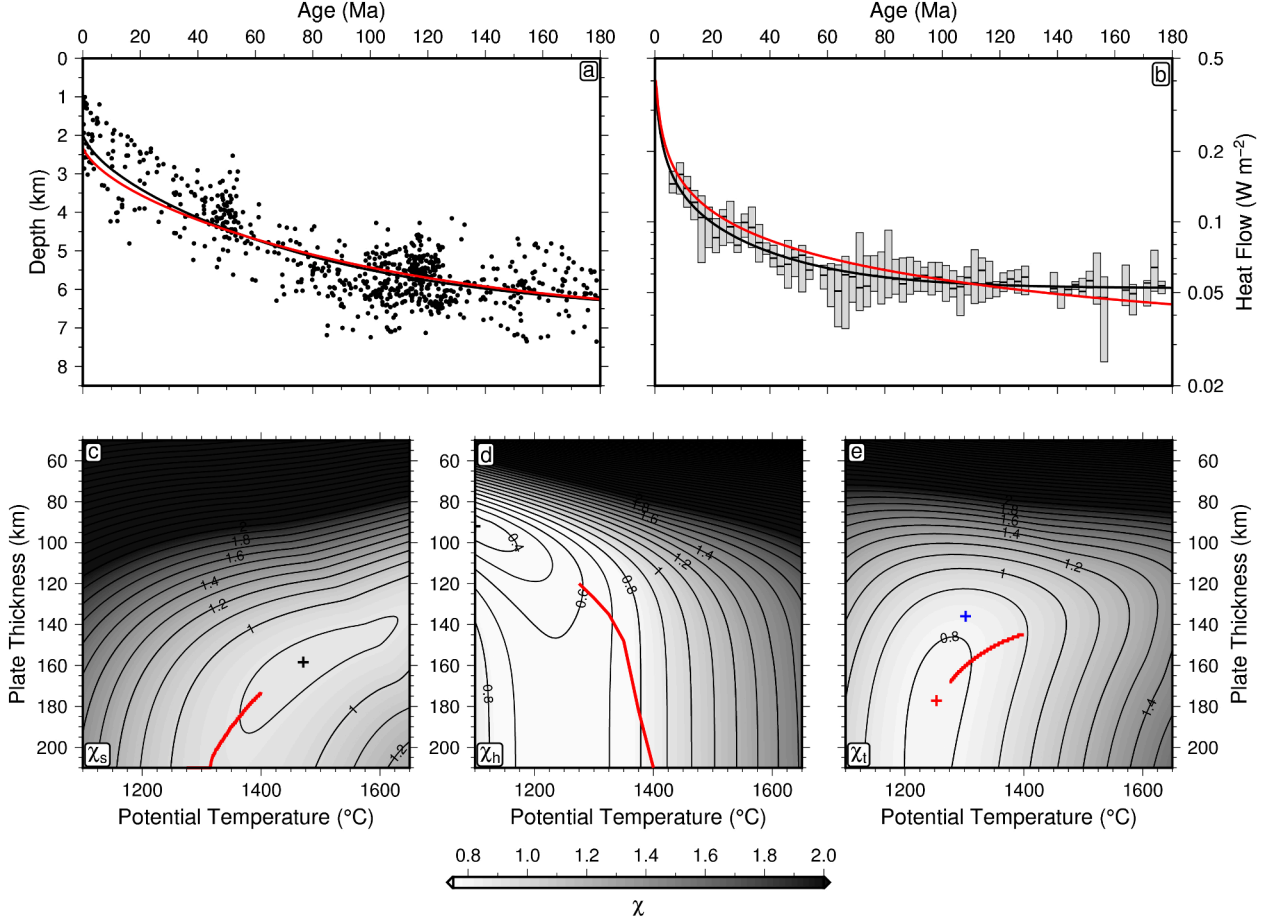


Figure S5: **Complete plate model with input data from Atlantic Ocean only.** (a) Water-loaded depth to oceanic basement as function of plate age (Figure 2d); black line = optimal relationship obtained by only fitting age-depth observations; red line = optimal relationship from joint fit of age-depth and heat flow observations. (b) Surface heat flow as function of plate age (Figure 3c); gray boxes with horizontal bars = interquartile ranges of sediment-corrected heat flow measurements and median values; black line = optimal relationship obtained by only fitting heat flow observations; red line = optimal relationship from joint fit of age-depth and heat flow observations. (c) Misfit between observed and calculated age-depth observations, χ_s , as function of potential temperature and plate thickness, sliced at best fitting zero-age depth of 2.00 km; black cross = misfit minimum; red cross = joint misfit minimum used to generate red curves in panels (a) and (b); red bar = optimal parameters when axial temperature is fixed at $1340 \pm 60^\circ\text{C}$. (d) Same for misfit between observed and calculated heat flow, χ_h . (e) Same for joint misfit, χ_t , between observed and calculated age-depth and heat flow observations, sliced at best fitting zero-age depth of 2.35 km; red cross = global minimum used to generate red curves in panels (a) and (b); blue cross = global minimum of global dataset.

Complete Half-Space Cooling Model

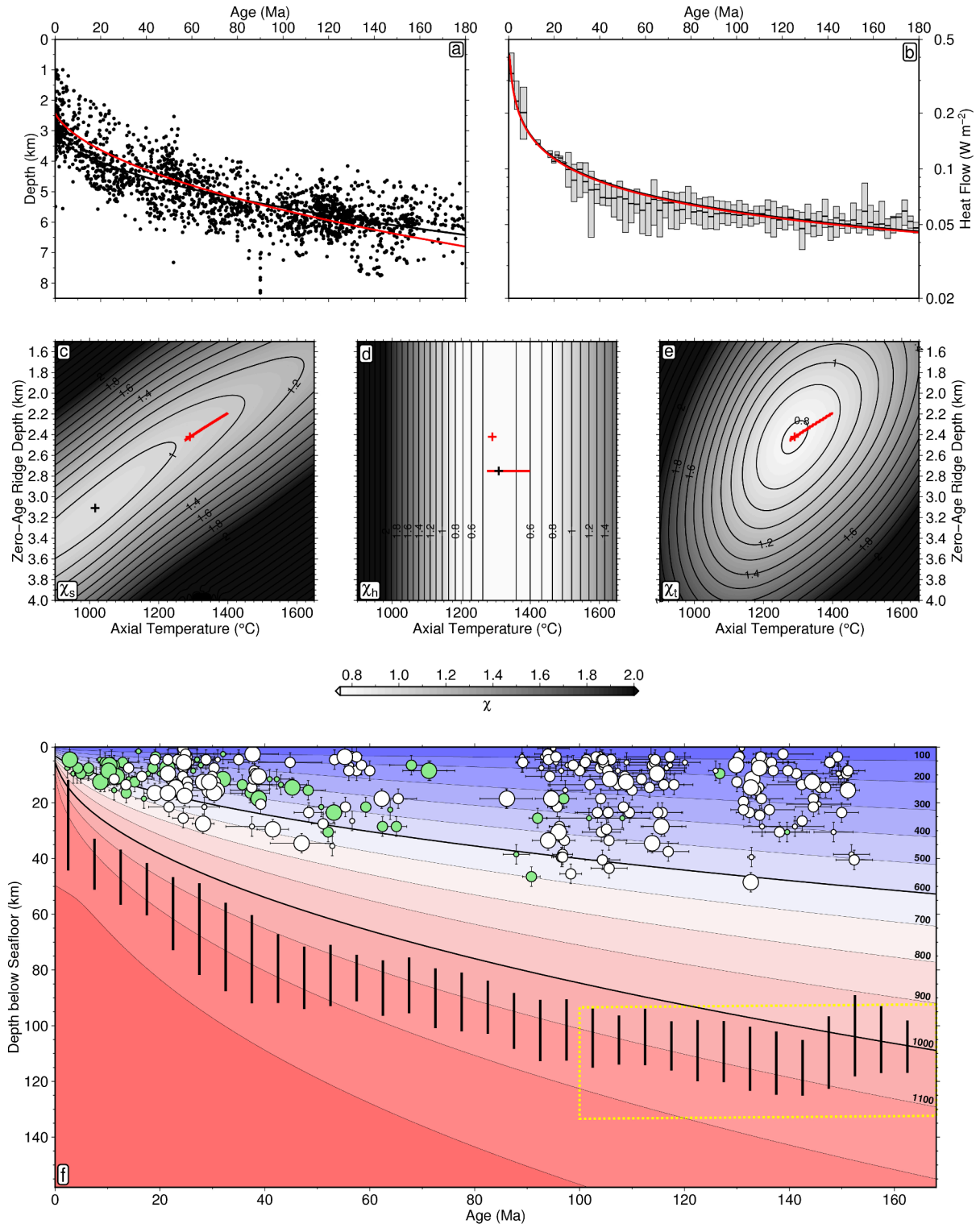


Figure S6 (*previous page*): **Temperature-and pressure-dependent half-space cooling model including 7 km oceanic crustal layer.** (a) Water-loaded depth to oceanic basement as function of plate age (Figure 2d); black line = optimal relationship obtained by only fitting age-depth observations; red line = optimal relationship from joint fit of age-depth and heat flow observations. (b) Surface heat flow as function of plate age (Figure 3c); gray boxes with horizontal bars = interquartile ranges of sediment-corrected heat flow measurements and median values; black line = optimal relationship obtained by only fitting heat flow observations; red line = optimal relationship from joint fit of age-depth and heat flow observations. (c) Misfit between observed and calculated age-depth observations, χ_s , as function of axial temperature and zero-age ridge depth, sliced at best fitting zero-age depth of 3.15 km; black cross = misfit minimum; red bar = optimal parameters when axial temperature is fixed at $1340 \pm 60^\circ\text{C}$. (d) Same for misfit between observed and calculated heat flow, χ_h . (e) Same for joint misfit, χ_t , between observed and calculated age-depth and heat flow observations, sliced at best fitting zero-age depth of 2.42 km; red cross = global minimum used to generate red curves in panels (a) and (b). (f) Predicted thermal structure of oceanic lithosphere. Numbered contours = isothermal surfaces plotted in $^\circ\text{C}$; green and white circles with error bars = oceanic intraplate and outer rise earthquakes from *Craig et al.* (2014) where small/medium/large circles = $M_b < 5.5$, $5.5\text{--}6.5$ and > 6.5 ; vertical black bars = depth to lithosphere-asthenosphere boundary in the Pacific Ocean based upon peak variations in azimuthal anisotropy (*Burgos et al.*, 2014); dashed box = envelope of depths to lithosphere-asthenosphere boundary for plate ages > 100 Ma (*Steinberger and Becker*, 2016).

Seismogenic Thickness and LAB Predictions

Table S1: **Comparison of thermal structure and seismic constraints.** T_S = seismogenic thickness-controlling isotherm for best-fit models; $[T_S]_{1333\text{ }^\circ\text{C}}$ = seismogenic thickness-controlling isotherm for geochemically constrained models. z_L = average depth at $t \geq 100$ of T_L isotherm where $\phi = 0.843$ for best-fit models; $[z_L]_{1333\text{ }^\circ\text{C}}$ = average depth at $t \geq 100$ Ma of T_L isotherm where $\phi = 0.843$ for geochemically constrained models; upper and lower bounds correspond to $\phi = 0.9$ and $\phi = 0.78$, respectively. Model name abbreviations same as in Table 1.

Model	T_S ($^\circ\text{C}$)	$[T_S]_{1333\text{ }^\circ\text{C}}$ ($^\circ\text{C}$)	z_L (km)	$[z_L]_{1333\text{ }^\circ\text{C}}$ (km)
HSCk	728	653	132^{+20}_{-16}	131^{+20}_{-16}
Pk	760	685	96^{+7}_{-7}	82^{+5}_{-6}
MR*	630	606	90^{+4}_{-5}	88^{+4}_{-5}
KR	473	561	107^{+7}_{-8}	113^{+7}_{-8}
KRC	486	588	114^{+9}_{-10}	118^{+10}_{-10}
KRCCK	743	754	113^{+10}_{-10}	114^{+5}_{-11}
KRCC	694	706	109^{+10}_{-10}	110^{+10}_{-10}

Comparison with Previously Proposed Thermal Models

Table S2: **Summary of previously published model results.** PS77 = *Parsons and Sclater* (1977); SS92 = *Stein and Stein* (1992); MJP05 = *McKenzie et al.* (2005); GA13 = *Grose and Afonso* (2013); KK16 = *Korenaga and Korenaga* (2016); RHCW18 = this study (KRCC model). * Fit is only calculated up to 100 Ma as model prediction is truncated at this age – others misfit calculations are carried out up to 170 Ma.

Model	χ_s	χ_{hf}	χ_t
PS77	0.947	1.035	0.992
SS92	1.007	0.446	0.779
MJP05	0.933	0.608	0.787
GA13	0.946	0.607	0.795
KK16*	1.419	0.520	1.069
RHCW18	0.931	0.442	0.729

Optimal Models for Subsidence and Heat Flow Datasets

Table S3: **Summary of results for fitting of subsidence and heat flow datasets separately.** Optimal parameters, where T is a free parameter, for subsidence data (labelled with $[X]_s$ subscripts) and heat flow data (labelled with $[X]_{hf}$ subscripts). Model name abbreviations same as in Table 1.

Model	$[T_P]_s$ ($^{\circ}\text{C}$)	$[z_p]_s$ (km)	$[z_r]_s$ (m)	χ_s	$[T_P]_{hf}$ ($^{\circ}\text{C}$)	$[z_p]_{hf}$ (km)	χ_{hf}
HSCk	1005	—	2816	0.951	1503	—	0.624
Pk	1307	129	2352	0.927	1474	92	0.416
MR*	1221	110	2548	0.927	1379	85	0.407
KR	1067	141	2432	0.927	1090	104	0.413
KRC	1147	151	2444	0.927	1086	112	0.410
KRCCK	1308	136	2684	0.928	1310	142	0.444
KRCC	1325	136	2604	0.927	1304	140	0.441

Notation Table

Table S4: Notation table for parameters used in text.

Notation	Parameter	Dimensions/Value
A	seafloor area	m^2
α	thermal expansivity	K^{-1}
C_p	specific heat capacity	$\text{J kg}^{-1} \text{K}^{-1}$
F	fractional disturbance of heat flow	dimensionless
G	gravitational constant	$6.67 \times 10^{-11} \text{ m}^3 \text{ kg}^{-1} \text{ s}^{-2}$
Δg	gravity anomaly	m s^{-2}
H	heat flow	W m^{-2}
k	thermal conductivity	$\text{W m}^{-1} \text{K}^{-1}$
k_{lat}	lattice thermal conductivity	$\text{W m}^{-1} \text{K}^{-1}$
k_{rad}	radiative thermal conductivity	$\text{W m}^{-1} \text{K}^{-1}$
κ	thermal diffusivity	$\text{m}^2 \text{s}^{-1}$
l	spherical harmonic degree	dimensionless
λ	longitude	$^\circ$
Q	cumulative oceanic heat flow	TW
m	spherical harmonic order	dimensionless
P	pressure	Pa
ϕ	critical isotherm coefficient	dimensionless
R	Earth radius	6371 km
ρ	density	kg m^{-3}
ρ_b	density at compensation depth	kg m^{-3}
ρ_m	mantle density	kg m^{-3}
ρ_w	water density	kg m^{-3}
S	sedimentation rate	m s^{-1}
t	time	s
Δt	finite difference timestep	s
ΔU	gravitational potential anomaly	$\text{m}^2 \text{s}^{-2}$
T	temperature	$^\circ\text{C}$
T_0	surface temperature	$^\circ\text{C}$
T_L	critical isotherm defining lithospheric thickness	$^\circ\text{C}$
T_p	mantle potential temperature	$^\circ\text{C}$
θ	co-latitude	$^\circ$
X	composition	dimensionless
χ_{hf}	heat flow misfit	dimensionless
χ_s	subsidence misfit	dimensionless
χ_t	joint misfit	dimensionless
z_c	crustal thickness	km
z_p	plate thickness	km
z_r	zero-age ridge depth	m
Δz	finite difference depth spacing	m
w	water-loaded oceanic basement depth	m

References

- Burgos, G., J. P. Montagner, E. Beucler, Y. Capdeville, A. Mocquet, and M. Drilleau (2014), Oceanic lithosphere-asthenosphere boundary from surface wave dispersion data, *J. Geophys. Res. Solid Earth*, *119*(2), 1079–1093, doi:10.1002/2013JB010528.
- Craig, T. J., A. Copley, and J. Jackson (2014), A reassessment of outer-rise seismicity and its implications for the mechanics of oceanic lithosphere, *Geophys. J. Int.*, *197*(1), 63–89, doi:10.1093/gji/ggu013.
- Grose, C. J., and J. C. Afonso (2013), Comprehensive plate models for the thermal evolution of oceanic lithosphere, *Geochemistry, Geophys. Geosystems*, *14*(9), 3751–3778, doi:10.1002/ggge.20232.
- Korenaga, T., and J. Korenaga (2016), Evolution of young oceanic lithosphere and the meaning of seafloor subsidence rate, *J. Geophys. Res. Solid Earth*, *121*, 6315–6332, doi:10.1002/2016JB013395.
- McKenzie, D., J. Jackson, and K. Priestley (2005), Thermal structure of oceanic and continental lithosphere, *Earth Planet. Sci. Lett.*, *233*(3-4), 337–349, doi:10.1016/j.epsl.2005.02.005.
- Müller, R. D., M. Sdrolias, C. Gaina, and W. R. Roest (2008), Age, spreading rates, and spreading asymmetry of the world’s ocean crust, *Geochemistry, Geophys. Geosystems*, *9*(4), doi:10.1029/2007GC001743.
- Müller, R. D., M. Seton, S. Zahirovic, S. E. Williams, K. J. Matthews, N. M. Wright, G. E. Shephard, K. T. Maloney, N. Barnett-Moore, D. J. Bower, and J. Cannon (2016), Ocean basin evolution and global-scale reorganization events since Pangea breakup, *Annu. Rev. Earth Planet. Sci. Lett.*, April, 107–138, doi:10.1146/annurev-earth-060115-012211.
- Parsons, B., and J. G. Sclater (1977), An analysis of the variation of ocean floor bathymetry and heat flow with age, *J. Geophys. Res.*, *82*(5), 803, doi:10.1029/JB082i005p00803.
- Stein, C. A., and S. Stein (1992), A model for the global variation in oceanic depth and heat flow with lithospheric age, *Nature*, *356*, 133–135, doi:10.1038/359123a0.
- Steinberger, B., and T. W. Becker (2016), A comparison of lithospheric thickness models, *Tectonophysics*, doi:10.1016/j.tecto.2016.08.001.